Specific Loss Power Optimization in Metal Ferrite Nanocrystals for Radiofrequency Stimulation of Neurons

by

Nathan S. Lachenmyer

Submitted to the Department of Electrical Engineering and Computer Science
in partial fulfillment of the requirements for the degree of

Master of Engineering in Electrical Engineering and Computer Science

at the

MASSACHUSETTS INSTITUTE OF TECHNOLOGY

September 2012
[February 2013]

Author . . . .
Department of Electrical Engineering and Computer Science
September 7, 2012

Certified by . . . .
Prof. Polina O. Anikeeva
AMAX Assistant Professor in Materials Science and Engineering
Thesis Supervisor

Accepted by . . . .
Prof. Dennis M. Freeman
Masters of Engineering Thesis Committee

Specific Loss Power Optimization in Metal Ferrite Nanocrystals for Radiofrequency Stimulation of Neurons

by

Nathan S. Lachenmyer

Submitted to the Department of Electrical Engineering and Computer Science
on September 7, 2012, in partial fulfillment of the
requirements for the degree of
Master of Engineering in Electrical Engineering and Computer Science

Abstract

Neurons serve as the basic unit of computation within the nervous system. As the nervous system is involved with the encoding, transmission, processing, and decoding of information at every level, characterization of the nervous system is of the utmost interest to neuroscience. However, techniques for probing the nervous system have previously focused primarily of characterizing single cell behavior, which does not provide insight as to the functioning of the system as a whole. This is further complicated by the fact that functional network of neurons are typically spatial interwoven, rendering spatially-limited stimulation techniques ineffective. The desire to characterize the system in its entirety necessitates the development of neuronal probes that can target functional subpopulations of cells. A proposed system for such stimulation is the genetic targeting of neurons via expression of gated ion channels, and the selective stimulation of them using a transmitter-receiver pair.

This thesis describes the design and optimization of such a transmitter-receiver pair that activates ion channels via the dissipation of heat. Magnetic losses in superparamagnetic metal ferrite nanocrystals are modeled to determine the optimal operating parameters for dissipation of heat. Optimal nanocrystals are then synthesized via high-temperature thermolysis of a mixed metal oleate precursor, and stabilized in the aqueous phase through functionalization with polyethylene glycol. A solenoid is designed and constructed to serve as a radiofrequency excitation source, and subsequently optimized to maximize the power transfer from solenoid to magnetic nanocrystals. A susceptometer and lock-in amplifier are designed for characterization of colloidal nanocrystals in the aqueous phase. The constructed susceptometer is then used to measure magnetic losses in metal ferrite nanocrystals and compare their performance with the modeled behavior.

Thesis Supervisor: Prof. Polina O. Anikeeva
Title: AMAX Assistant Professor in Materials Science and Engineering

Acknowledgments

First and foremost, I would like to thank Professor Polina Anikeeva for providing me with the opportunity to work on this project. She provided me not only with the opportunity to challenge myself with this project, but with the independence to choose my own route to completion. Likewise, I would like to thank the rest of the Bioelectronics group for their support and teamwork the past year. This project has taught me countless invaluable lessons about teamwork and project management.

I would like to thank Mike Tarkanian, Matt Humbert, David Bono, and Mark Feldmeier for both their professional and personal support during the completion of this project. Without their continued support, the vast majority of this work simply could not have happened. In addition, Cruft Laboratories and its community has provided me with outlets that were invaluable to my sanity during the writing of this thesis. I am thankful for their continued support.

Contents

List of Figures

Chapter 1

Introduction

1.1 Background

Bioelectric phenoma of the cell are among the most vital functions of a living organism. Bioelectric phenomena are used to drive transport, sensing, transduction, and metabolic regulation within various cells. In addition to their paramount importance within the living cell, bioelectricity provides a method for characterizing biological systems. While biochemical or biophysical phenomena cannot be measured directly, their indirect effects on bioelectrical systems can be measured easily with electrodes and standard signal processing techniques.

As early as 1791, when Luigi Galvani used a Leyden jar to stimulate the femoral nerve of a frog[Gal91], scientists have directly stimulated neurons to study their function. Nearly 50 years later, Carlo Matteucci measured bioelectric currents using galvonometers[Mat38], marking the first bioelectric recording and spawning the field of electrophysiology. As technology and biology advanced, electrophysiological measurements became more specific, allowing measurements to be made on single cells and confirming theoretical foundations of cell biology. In 1976, the patch clamp technique was invented by Erwin Neher and Bert Sakmann[NS76], allowing electrophysiological measurements of single ion channels. This technique allowed the integration of molecular biology with electrophysiology for the first time, giving insight as to the origins of bioelectrical phenomena.

In contrast to the high level of precision available through electrophysiological measurement techniques, bioelectrical stimulation techniques are remarkably imprecise. Artificial stimuli are often delivered via electrodes, allowing only coarse spatial targeting of cellular populations. In the case of neuroscience, specific classes of neurons tend to be sparsely embedded within tissue, making it extremely difficult to target functional, rather than spatial, populations of cells. The ability to precisely stimulate a given functional population of neurons would allow neuroscience to move from observation-based studies to experimental studies, where the behavior of a given subpopulation of neurons could be resolved in isolation.

A particularly elegant solution is to equip targetted cells with a 'receiver' that allows a response to an otherwise spatial signal. In this manner, cells within the same spatial region that lack a receiver will ignore the stimulus, but the targetted cells will respond. Such a receiver can be encoded genetically, allowing for functional subpopulations of neurons to be targetted.[Cri99][ZM01] Of particular interest is photostimulation of neurons that express light-activated ion channels[ZLNM02][BZB$^+$05][CK08].

Photostimulation of these light-sensitive ion channels is limited by the depth that the requisite radiation can penetrate into bone and tissue. However, magnetic fields interact weakly with biological materials and are relatively simple to create and operate, making them an ideal candidate for stimulation of neurons deep within tissue. However, their weak interactions also require the need for a magnetic transducer that can convert the energy of the magnetic field into an electrical potential across the cell membrane.

This thesis proposes such a system and lays down the groundwork for progress in this growing field. The proposed system uses superparamagnetic nanocrystals as magnetic transducers to convert energy from the radiation field to thermal energy via magnetic losses. Neurons are genetically targeted to express the TRPV1 ion channel, which is heat sensitive. The nanocrystals are bounded to the heat-sensitive ion channels via functionalization of the nanocrystal surface, and the magnetic losses cause the channel to open. Calcium imaging and patch clamp electrophysiology are used to demonstrate the depolarization of the membrane.

1.2 Overview

Chapter 2 presents the relevant cell biology theory. This chapter describes in detail the relevant aspects of neuron molecular biology and the kinetics of the transient receptor potential vallinoid (TRPV) ion channels.

Chapter 3 details the optimization of our framework described in Chapter 3. The theory behind inductive heating of magnetic nanocrystals is explored and simulated to determine the optimal operating parameters and nanoparticle synthesis techniques. The heating power of various nanoparticle chemistries are measured.

Chapter 4 describes the synthesis, stabilization, and characterization of nanocrystalline receivers for neuronal stimulation.

Chapter 5 describes the design and construction of a radiofrequency coil capable of producing magnetic fields suitable for *in vivo* and *in vitro* cell stimulation.

Chapter 6 presents experimental results. Using the apparatus described in Chapter 5, the magnetic losses are directly measured as quadrature susceptabilities in colloidal nanocrystals. The results are compared to the theory described in Chapter 3.

Chapter 7 concludes with a discussion of our experimental results, and an outlook on future experiments in this field.

1.3 Contributions

The work described in this manuscript was performed in Professor Polina Anikeeva's laboratory in the Department of Materials Science and Engineering at the Massachusetts Institute of Technology. Ritchie Chen and Moises Montalvo performed the synthesis of colloidal nanocrystals, including developing the aqueous phase stabilization protocol. David Bono assisted with the construction of the excitation source and provided many helpful discussions while designing the lock-in amplifier described in Section 5.2.2.

Chapter 2

Membrane Biology

In this manuscript, we concern ourselves with how to actuate this regulatory system to control the bioelectric behavior of cells. In order to

We seek to implement a system that can overcome the shortcoming of optogenetics. Therefore, the proposed system must utilize a stimuli that can induce fast, selective responses in populations of neurons while also allowing for deep tissue stimulation. In addition, we prefer that the ion channel be mammalian in origin.

2.1 Information Encoding in Biological Systems

Electric potentials within the cell are involved in many cellular processes. The most important of these processes is the encoding of information in the nervous system. The nervous system is responsible for the encoding, transmitting, processing, and decoding of information that is received as optical, mechanical, electrical, or chemical stimuli and transducing these signals into an electric potential. The electric potential serves as the common mode of communication between cells with which they represent information. These electrical signals are ultimately processed and converted into motor or secretory responses.

The neuron is the basic unit of the nervous system, responsible for directly transmitting and receiving electrical signals in addition to performing computations on the information provided. These cells are electrically active; when a current of sufficient strength is passed through the plasma membrane (thus depolarizing the membrane), a change in the membrane potential called an action potential is triggered. The sudden onset of an action potential causes the membrane to hyperpolarize through the sudden diffusion of ionic species (predominantly Na^+ and Ca^{2+}) in and out of the membrane; this sudden change causes a cascade of ionic flux within the cell, creating a pulse of electric energy. This pulse propagates from the cell body, down the axon, and through the axonal terminals. From the axonal terminals, the signal can be transferred to another cell via a synaptic site on the surface of an adjacent dendrite. Each neuron may contain only a single synaptic input or as many as thousands, and may receive them along the dendrites or the cell body; it is the spatiotemporal distribution of synaptic activity and how the neuron processes it that produces such varied and complex behavior.

The human nervous contains over 10^{11} neurons arranged in a complex, highly structured network.[Wei96] Subnetworks exist that perform such specialized tasks as motor control, auditory sensing, and communication between internal organ systems. Each subnetwork is composed of heterogeneous populations of nerve cells possessing different structures and functions. The vast complexity of the neuronal network makes the correlation between cellular signals and organismic behavior extremely difficult to isolate. Progress has been made in understanding the basis of organismic behavior in only the simplest of invertebrates (e.g. C. elegans) where the behavior is determined by a small number of neurons that can be unambiguously identified and isolated; however, even in these cases only the simplest behaviors have been understood.[BK78]

Substantial progress has been made in understanding the structure and function of neurons through studying technically favorable models (such as the squid giant axon[You38]), resulting in complete models of single neuron behavior.[HHK52] However, these simple cellular models do not adequately capture the dynamics of a complex neuronal network because information is often carried by neural ensembles rather than single neurons. Even in favorable neuroanatomical circumstances studying such transient functional linkages between neurons has proven to be a substantial experimental challenge. As a consequence, modern neurobiology research has focused on experimental techniques that allow for the selective targetting and virtual isolation of neural pathways.

2.2 Cell Biology

Recent developments in experimental neurobiology have turned to using genetic schemata to achieve such selectivity.[ZM01] Modern genetics has allowed for the determination of regulatory elements responsible for gene expression; once these patterns have been identified and isolated, they can be used to exogeneously express natural or engineered proteins within neurons. These proteins can be selected to report, interface, or interfere with neural physiology in a controlled manner. In order to target functional populations of neurons, it is reasonable to begin with one of the more fundamental surface proteins involved with neuronal behavior: the ion channel.

2.2.1 Plasma Membrane

All livings cells are surrounded by a plasma membrane that acts as a divider between the cytoplasm and the extracellular media. The membrane serves to both physically and chemically isolate the cell from its environment, ensuring tight control over all intracellular processes. In order to maintain such tight control, the membrane is host to a variety of channels, carriers, and pumps that serve to regulate the molecular contents of the cell. These proteins function to control the structure, signaling, and homeostasis of the cell through a careful network of regulatory hormones and signals.

Of particular importance is the gradient of ions across the membrane. A membrane potential arises when there exists a difference in charge on opposing sides of the membrane due to an excess of positive ions on one side of the membrane and an excess of anions on the other side. This situation occurs in cells due to the presence of permanent organic anions present within the membrane and electrodiffusive equilibrium placing more cations outside of the cell membrane. This membrane potential stores energy that can be used in a variety of ways within the cell. Neurons use rapid variations in the membrane potential to transmit information in the form of action potentials; biological sensors in the visual and auditory systems utilize the membrane potential to transduce external stimuli into information that cells can process; and is even involved in the regulation of homeostasis.

The concentration gradient of ionic species across the membrane is responsible for two separate mechanisms of transport. The first one is diffusion, where the ionic species diffuse from high concentration to low concentration until an equilibrium is achieved due to a uniform spatial distribution across the membrane. However, the fact that ionic species possess a charge creates an opposing electrostatic force due to the accumulation of charge. For example, potassium (which is concentrated within the cell but dilute outside of the membrane) will tend to diffuse out of the cell due to the concentration gradient; however, with each potassium ion that leaves the cell, the intracellular space begins to become more negatively charged than the extracellular space. This negative charge attracts potassium ions back against the concentration gradient. A steady-state equilibrium is reached when the electrostatic forces and the diffusive forces are equal.

The flow of ions across the plasma membrane is facilitated by a variety of specialized proteins. They are primarily sorted into two categories: passive and active transport proteins. Passive transport proteins, such as ion channels, are composed of an aqueous pore that allows for diffusion of an ionic species across the membrane (see Figure 2-1. Nearly all ion channels possess a gating mechanism to determine whether the pore is open or closed. Active transport consist of specialized proteins that facilitate the transport of ionic species against their concentration gradient. These proteins typically require an energy source to initiate transport; this energy is acquired either through the breakdown of cellular energy sources such as ATP, or through the co-diffusion of another chemical species along its concentration gradient.

2.2.2 Ion Channels

While the plasma membrane serves to isolate the cell from its environment, ion channels serve to provide a pathway between the intracellular and extracellular spaces.

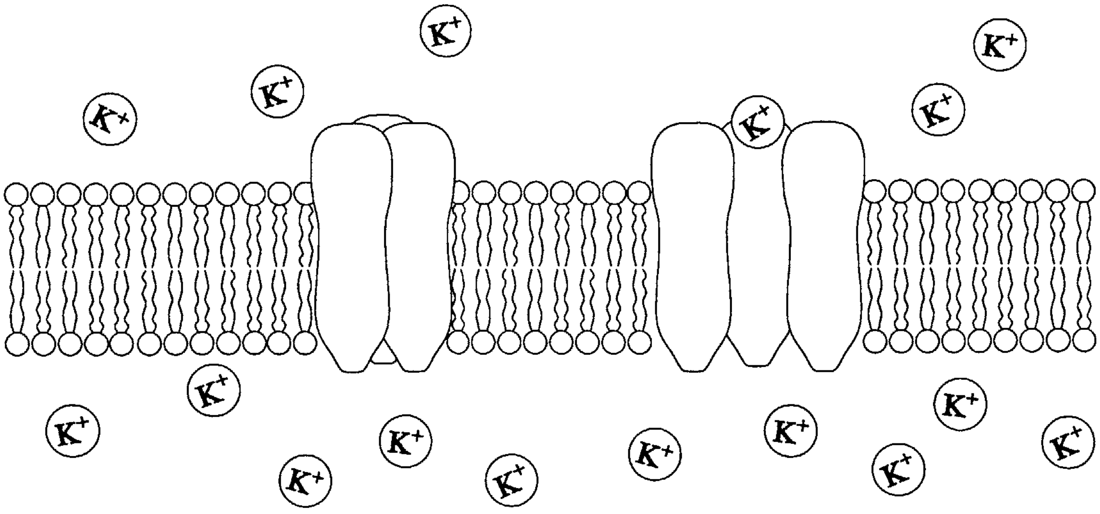

Figure 2-1: Schematic of an ion channel, embedded in the plasma membrane. The channel is shown open on the right and closed on the left.

These proteins are responsible for establishing the concentration gradient of various ionic species by varying the membrane's permeability to said species. Ion channels are ideal for this task because they possess three main properties:

1. A hydrophillic pore that allows the transport of aqueous ions.
2. Selective permeability to particular ionic species through variation in the size and charge of the pore.
3. A gating mechanism to change the state of the pore (open or closed).

The third property of ion channels is of particular interest because it suggests that a particular stimuli can be used to open or close an ion channel. The gating of an ion channel is based upon the conformational change of the channel protein initiated by a range of factors specific to the ion channel. There exists a diverse set of stimuli that can gate an ion channel – there are ion channels that are gated by electric potential, specific chemicals, pH, and mechanical stress, to name but a few. Modern genetics has given us the ability to bestow a large variety of proteins to cells; this allows us to expand our potentially targets beyond endogenously expressed ion channels. It is clear that with the appropriate stimulus, action potentials can be easily initiated and allow the control of information transfer within a biological system.

Voltage-gated ion channels are perhaps the most common of gated ion channels. These channels consist of charged pore proteins that shift conformation and open or close the pore in response to the membrane potential. These channels are also directly responsible for action potential amplification and propogation; when a small patch of membrane achieves the threshold voltage for an action potential, it activates nearby voltage-gated channels. This causes a cascade effect that enables detriment-free signal propogation in neurons. Due to a combination of their ubiquity and direct effect on the electric behavior of cells, voltage-gated ion channels have been used to stimulate neurons for over a century.[Gil05] Although the technology has advanced significantly since these first neuromodulators, the basic principle has been the same: an electrode is placed into tissue and the electrode transduces electric currents into ionic currents through the medium. Despite the demonstrated efficacy of such methods, voltage-gated ion channels are not ideal targets due to the spatial dependency of the stimuli. The spatial targetting abilities of direct electric stimulation are limited to the volume directly adjacent to the electrode, necessitating the need for implantable microelectrode arrays to allow for precision cell targetting. Even with such a microelectrode array, the affected zone is limited by the size of the array. For these reasons we find voltage-gated channels an unsuitable target channel.

A second type of gated ion channel is the ligand-gated channel. This group of ion channels is particularly rich, with not only a variety of ionic species affected by such channels, but also a vast array of stimulating chemicals available. These ion channels are especially prevalent in sensory systems, such as the gustatory system,[SB83] and in the nervous system, such as in the case of neurotransmitters.[DHK71] These ion channels are more favorable than voltage-gated channels because their stimuli are much more selective; agonists and antagonists can be selected for a cell subtype, and functional populations of cells can be targetted in this manner. However, these stimuli still suffer from spatial and temporal limitations; methods of delivering such chemical stimuli rely on diffusion to deliver the ligand to the cell's membrane, providing only very coarse temporal and spatial control over the stimuli. Once delivered, there currently lacks a scheme for deactivating excess ligands; therefore this method does not allow for fine temporal control.

The optical caging technique was developed to overcome many of these shortcomings; in this technique a 'caged' compound is used that becomes neuroactive upon exposure to light.[FG83] This allows for diffusion of the desired ligands to occur first, and then laser light can uncage the compound through photolysis. This allows for temporal control rivaling that of electrical stimulation[GCOZ97] while providing the benefits of substantially high selectivity of the stimuli. Nonetheless, optical caging suffers from a variety of technical limitations. While caged ligands can spatially select for desired cells, the requisite optics can only target a single location at a given moment; the ability to target multiple cells that are spatially separated requires the use of high-speed optics to scan over the sample. In addition, the requisite wavelength for uncaging is typically in the ultraviolet regime, which is undesirable because of its mutagenic side effects and requires the use of expensive ultraviolet optics. Lastly, the technique is similarly as invasive as direct electrical stimulation because direct optical access is needed, making the technique undesirable for *in vivo* applications.

The sole use of light to elicit an electrical response has many potential benefits. Light can be projected onto tissue with extremely precise spatial and temporal control, unlike electrical probes or extracellular ligands. Ion channels that are directly gated by optical irradiation also allow for transient stimulation via rapid pulses of light; this allows for precise sequencing of membrane depolarizations. Optically initiated depolarization in opsins can be triggered by visible wavelengths, making the optics much more practical than those used in optical caging; however, the lack of such proteins outside of the retina requires the exogenous expression of an opsin-related photoprotein.[CK08] The required exogenous expression is not necessarily a drawback; the fact that cells must be targetted specifically is indeed a benefit, as it allows subpopulations of neurons to be genetically targetted by function rather than spatial location.

The primary drawback of these light-gated channels are their slow kinetics; the optical response of most opsins is typically on the order of seconds, limiting their usefulness. The application of channelrhodopsin 2, which has kinetics almost a thousand times faster than most related opsins, has largely overcome many of the drawbacks of light-gated ion channels, making optogenetic stimulation (as the combination of pulsed lights with exogenously expressed light-gated channels has come to be called) the de facto standard for minimally invasive neuronal stimulation.[BZB+05] This method still requires optical access to the neuronal population, typically in the form of a surgically implanted optical fiber, making the technique suboptimal for in vivo applications where a less invasive technique may be preferred. The near-IR window provides a range of wavelengths (between 850 nm and 1.0 μm) where tissue absorption is at a minimum and transmission is at a maximum; this suggests that an infrared light-gated ion channel would provide a way to stimulate deep tissue neurons in a less invasive manner.

Mechanosensitive ('stretch-activated') ion channels are commonplace in the skin, muscles, tendons, and joints. These ion channels, as their name suggests, are gated by mechanical stimulation applied to the membrane. Work has been done in conjugating ferrite microparticles to bind specifically to these channels; a magnetic field can subsequently be applied to the cell to load the membrane and induce depolarization.[GFM95] By specifically targetting a protein on the membrane surface (as opposed to the entire cell), single channels can be actuated without interfering with the behavior of neighboring channels in the cell's membrane.[HMDH08] The use of magnetic fields as the energy delivering medium allows for deep tissue penetration where optical wavelengths would otherwise be fully attenuated. Nevertheless, mechanical stimulation has been demonstrated to give inconsistent results, likely due to the magnetic particles loading the membrane at a variable axis. Hughes et. al suggest that improved performance may occur with uniaxial loading of the membrane. Furthermore, the large microparticle size necessary for mechanical stimulation (1-10 μm) is unsuitable for *in vivo* applications.

Similar work has been done using magnetic nanocrystals as cellular transducers to convert energy from a radiofrequency field to electrical energy; rather than using mechanosensitive ion channels, the target is a temperature-gated ion channel in the transient receptor potential vanilloid (TRPV) family.[HDZ+10] Nanocrystals are conjugated to bind to the temperature-gated proteins and through magnetic losses dissipate energy from the radiofrequency field as heat. This shares many of the advantages of using a magnetic field as a mediator of energy rather than visible light; however, the literature shows that this method is far too slow for neural stimulation (taking approximately 30 seconds to induce an action potential). Yet, significant work has been done in the field of magnetic hyperthermia, where magnetic losses in ferrite nanocrystals are used to induce apoptosis in cancerous cells, to optimize the heating power of such nanocrystals.[PJW+03][CGC10] Recent studies have shown that the heating power can be significantly increased through careful tuning of material parameters and morphology.[LJC+11] With substantial improvements that can be made to the technique readily available, it is not unrealistic to expect a significant decrease in the stimulation time from this technique.

2.2.3 Transient Receptor Potential Vanilloid Receptors

The mammalian sensory system is capable of discriminating a wide range of temperatures, ranging from noxious cold (< 8 °C) to noxious heat (> 52 °C).[VDW+04] Studies done in the past decade have shown that the principle temperature sensors of the nervous system all belong to the transient receptor potential (TRP) family of cation channels.[Cla03] Of these TRP channels, the transient receptor potential vanilloid (TRPV) subfamily is of particular interest for its sensitivity to innocuous heat.

The origin of the temperature-sensitive behavior is relatively obscure, with many hypothesized mechanisms ranging from temperature-sensitive ligand release (placing TRP proteins into the ligand-gated ion channel family) to true temperature-sensitive gating due to temperature-dependent protein conformations. While the true activation mechanism remains unknown, structural similarity to voltage-gated cation channels and dual-stimulus studies have suggested a mechanism where thermosensitivity arises from the difference in activation energies associated with voltage-dependent opening and closing.[VDW+04][TT05]

TRPV1 was the first isolated member of the transient receptor potential vanilloid subfamily, having been isolated through expression cloning with capsaicin as a ligand.[CST$^+$97] Although TRPV1 was initially discovered through the use of capsaicin as a stimulus, it was also found to be thermosensitive with a critical gating temperature of 43 °C. This is only 5 °C above ambient body temperature, making it an extremely attainable target for *in vivo* heating. The rise time of the depolarization in response to a change in external temperature was measured to be 6 ms, suggesting that the kinetics are suitable for rapid stimulation.[YLQ10] The same study found that channel deactivation is temperature-independent, further suggesting that this mechanism is ideal for thermal stimulation *in vivo.*

TRPV1 has been shown to be a nonselective cation channel, showing permeability to calcium, magnesium, sodium, and potassium ions. However, the channel shows a preferential permeability to calcium that is over nine times the permeability of sodium and five times the permeability of magnesium, suggesting that calcium is the primary charge carrier.[VDW$^+$04] This allows for direct monitoring of channel behavior through the use of a calcium indicator such as fura-2 or GCaMP.

TRPV1 has been found to be ubiquitous in the peripheral nervous sytem, having been found to be an important nociceptor sensitive to temperature, pressure, and pH[MXC04]. However, it has also been found to be expressed in the central nervous system, where it has been hypothesized to participate in a variety of vanilloid-sensitive pathways, suggesting a variety of previously unforeseen therapeutic applications.[MTC$^+$00][SCDM08] Its ubiquitous endogenous presence in the mammalian sensory system suggests that is may be involved in a diverse number of human disease states, suggesting that selective, noninvasive *in vivo* control over this protein could be extremely beneficial for treating such states.

The combination of an easily attainable stimuli, fast kinetics, and easy direct monitoring of the ion channel make TRPV1 a nearly ideal candidate for activation through remote-controlled heating. In addition, its ubiquitous presence in the mammalian nervous system presents a vast array of endogenous targets as well the the ability to easily introduce the ion channel to targetted cells.

2.3 Summary

In this chapter, we provided the background necessary to understand the motivation for this thesis. The role of neurons in information encoding was described, as well as the role of ion channels in their function. A suitable ion channel target was determined based on the criteria that the stimuli was to be non-invasive, allow for functional targetting of neurons (rather than spatial), and the ion channel possessed rapid activation kinetics. The transient receptor potential vanilloid (TRPV) family of ion channels was selected as a suitable target, with TRPV1 being chosen as the target protein for its easy monitoring, fast kinetics, and easily attainable stimulus: a local temperature increase of approximately 5 ° from body temperature.

Chapter 3

Specific Loss Power Optimization

A large heating power is desirable for a magnetically induced hyperthermia applications. Nanocrystals with a large heating power reduce the amount of material necessary and time required to achieve neuronal stimulation. We use a radiofrequency magnetic field as an excitation source to align magnetic moments, and heat is dissipated through relaxational phenomena. A thorough understanding of these relaxational loss phenomena allows us to select appropriate operating parameters for optimization of the radiofrequency magnetic field. In addition, material properties may be carefully tuned to maximize the dissipative power of the synthesized nanocrystals.

This chapters is concerned with the theoretical foundations of magnetic losses in metal ferrite nanocrystals. Simulations are performed to fully characterize the heating power as a function of all controllable parameters, and optimal conditions are selected. The heating power of various nanocrystals are then measured and compared with our simulations.

3.1 Losses in Magnetic Materials

Losses occurring in magnetic particles can be divided into three classes – hysteresis losses, relaxational losses, and resonance losses. Hysteresis losses arise from the alignment of magnetic moments within a magnetic material. When an external field is applied, the moments align themselves with the field, magnetizing the material. When the field is removed, the material is left with a remanent magnetization, with energy stored within the material in magnetic domain interactions. A coercive field must be applied to coerce the material back to zero magnetization. This process requires net work to be done, known as hysteresis losses. Below a critical diameter, metal ferrite nanocrystals possess only a single magnetic domain and hysteresis losses disappear (a state of magnetism called superparamagnetism).[HAd+98]

The magnetization is single domain materials can reverse through relaxational phenomena. For sufficiently small diameter nanocrystals, the anisotropy barrier is reduced to the point where it can be overcome by thermal fluctuations. For nanocrystals whose moment is aligned by an external field, this can lead to the field's energy being dissipated as heat. In this fashion the magnetization of the particle reverses while the physical particle remains motionless. This type of relaxation is known a Néel relaxation.[N49] A second type of relaxational loss is due to Brownian relaxation, where the particle physical rotates with the magnetic field. In this process the particle's physical rotation is impeded by the viscosity of its carrier fluid. The particle takes a characteristic time τ_B to rotate in the carrier; if the field is changing faster than this characteristic time, then particle's magnetization experiences hysteresis and dissipates heat through these so-called Brownian losses.[Bro63]

The final kind of loss is due to ferrimagnetic resonance, where the nanocrystal exhibits a sharp increase in the absorption of energy from the electromagnetic field at a specific frequency. However, this phenomena occurs in the GHz range where transmission in the human tissue is reduced to a fraction of a millimeter, rendering this phenomena undesirable for *in vivo* applications.[GR86]

For small metal ferrite nanocrystals, relaxational losses are the dominant mechanism through which energy is dissipated when exposed to an oscillating magnetic field.

3.1.1 Theory

From the first law of thermodynamics, it is possible to derive the amount of work done on a magnetic material under a changing external field as:[Ros02]

$$\Delta W = -\mu_0 \oint M dH \tag{3.1}$$

where M is the magnetization of the material (measured as the magnetic moment per volume) and H is the applied field. The magnetization and applied field are related by a proportionality constant χ, the magnetic susceptibility, such that $M = \chi H$. It is convenient for this discussion to represent the externally applied magnetic field $H(t)$ and the magnetization $M(t)$ as:

$$\begin{aligned} H(t) &= H_0 \cos(\omega t) && (3.2) \\ M(t) &= \chi H_0 \cos(\omega t) && (3.3) \\ M(t) &= H_0(\chi' \cos(\omega t) + \chi'' \sin(\omega t)) && (3.4) \end{aligned}$$

where H_0 is the field amplitude, ω is the angular frequency, and χ' and χ'' are the real and imaginary components of the magnetic susceptibility, respectively. Within the magnetization term, $\chi' \cos \omega t$ represents the component of the magnetization that is in-phase with the applied field, indicating the storage of magnetic energy. In contrast, $\chi'' \sin \omega t$ is the out-of-phase component that is proportional to losses (called the quadrature). Substituting into Equation 3.1:

$$\Delta W = 2\mu_0 H_0^2 \chi'' \int_0^{2\pi/\omega} \sin(\omega t)^2 dt \tag{3.5}$$

Following through with the integration and multiplying by the frequency of oscillation $f = \frac{\omega}{2\pi}$ gives the volumetric power dissipation, or volumetric loss power:

$$P = \mu_0 \pi \chi'' f H_0^2 \tag{3.6}$$

The power dissipated in dependent upon the amount of magnetic material present, so it is intuitive to divide it by the mass concentration of magnetic material i, γ_i to normalize it to a specific loss power:

$$q = \frac{\mu_0 \pi \chi'' f H_0^2}{\gamma} \tag{3.7}$$

where all of the material properties of the magnetic material are encapsulated in χ''. The loss component of the susceptibility is given by:[Shl74]

$$\chi'' = \chi_0 \frac{2\pi f \tau}{1 + (2\pi f \tau)^2} \tag{3.8}$$

such that χ_0 is the equilibrium susceptibility and τ is the relaxation time of the magnetic material. As discussed above, for magnetic nanocrystals there are two relaxation phenomena – Brownian and Néel relaxation. For Brownian relaxation, the relaxation time is given by:[Bro63]

$$\tau_B = \frac{3\eta V_H}{k_B T} \tag{3.9}$$

such that η is the viscosity of the carrier medium, V_H is the hydrodynamic volume (typically 1-3 nm larger than the nanocrystal volume), k_B is Boltzmann's constant (1.38×10^{-3} J K^{-1}), and T is the absolute temperature (in Kelvin). The other type of relaxation is Néel relaxation, which is defined as:[N49]

$$\tau_N = \tau_0 e^{-\frac{KV}{k_B T}} \tag{3.10}$$

where K is the anisotropy energy density (in J m^{-3}), V is the nanocrystal volume, and τ_0 is a constant on the order of 10^{-9} seconds. The two relaxation processes take place in parallel, giving rise the effective relaxation time:

$$\frac{1}{\tau} = \frac{1}{\tau_N} + \frac{1}{\tau_B} \tag{3.11}$$

Due to the parallel nature of the relaxation process, the faster of the two relaxation mechanisms tends to dominate the relaxation of the entire ensemble. The relaxation mechanisms indicate that there are three parameters that influence the loss power that are within our control – the anisotropy energy density K, the nanocrystal diameter d, and the carrier fluid viscosity η. The anisotropy energy density can be controlled by materials selection, whereas the diameter is controlled by our synthetic process. The fluid viscosity can be controlled for *in vitro* experiments, but for *in vivo* applications (especially applications where the nanocrystals are bound to the cell membrane) we have little control over the viscosity. Therefore, for considerations as to how to optimize the specific loss power, only the Néel relaxation mechanism is considered.

One may intuit that the optimal field parameters would depend on the relaxation time constant. If the excitation field is significantly slower than the relaxation process, then suboptimal heating is produced. The magnetic moment fully relaxes, dissipating heat, and then remains in its relaxed state until the field excites the magnetic moment again. In this case the magnetic moment spends excess time relaxed where it is not dissipating energy. In the case of an excitation source that is significantly faster than the relaxation time, suboptimal heating occurs because the magnetic moment does not fully relax before it is excited again. Therefore, optimal heating is produced when the excitation field frequency is equal to the relaxation time.

The equilibrium susceptibility may be derived from Langevin function:[Ros02]

$$\chi_0 = \frac{\mu_0 M_S^2 V}{\xi k_B T}\left[\coth\xi - \frac{1}{\xi}\right] \tag{3.12}$$

$$\xi = \frac{\mu_0 M_S H_0 V}{k_B T} \tag{3.13}$$

where M_S is the saturation magnetization of the nanocrystals (in A m^{-1}). We must note that the nomenclature for magnetization in magnetic fluids is ambiguous; the saturation magnetization M_S refers to the amount of magnetization per unit volume of magnetic material. However, in a magnetic fluid, a very small fraction of the fluid is actually magnetic – most of the fluid is a magnetically inert carrier fluid. To avoid confusion between the saturation magnetization of the magnetic fluid and the saturation magnetization of the magnetic particles, we rewrite the equations in terms of σ, the specific magnetization (in A m^2 per gram of magnetic material). This allows a straightforward measurement of the magnetization because the mass concentration γ is usually known in the preparation of a magnetic suspension.

Combining terms and rewriting in terms of σ, the equilibrium susceptibility can be simplified to:

$$\chi_0 = \frac{\sigma\gamma_i}{H_0}\left[\coth\xi - \frac{1}{\xi}\right] \tag{3.14}$$

$$\xi = \frac{\mu_0\sigma\rho H_0 V}{k_B T} \tag{3.15}$$

where ρ is the density of the magnetic material (in g m^{-3}). Thus, the specific loss power can be written as:

$$q = \mu_0\pi\sigma H_0 f\frac{2\pi f\tau}{1+(2\pi f\tau)^2}\left[\coth\xi - \frac{1}{\xi}\right] \tag{3.16}$$

The specific loss power explicitly depends on five factors that are directly related to the design of the transmitter and nanoantennae: the transmitter's field frequency and amplitude, and the nanocrystal's specific magnetization, anisotropy energy density, and diameter. The transmitter properties as easily controlled externally, the diameter is determined by the synthesis method, and the specific magnetization and the anisotropy energy density are determined by materials selection.

3.1.2 Modeling

The effect of each on the specific loss power is not straightforward due to complex dependencies on the material parameters, so it is instructive to explicitly determine the effect of each parameter on the losses. In this section we compute the specific loss power as a function of various tunable parameters to determine the optimal state to operate the remote stimulation system with.

In order to vary each parameter independently, we must define a standard set of values to hold the unvarying parameters to. These values, collected from the

Parameters	Standard Value
Field Frequency	500 kHz
Field Amplitude	5 kA m^{-1}
Particle Diameter	10 nm
Specific Magnetization	0.06 A m^2 g^{-1}
Anisotropy Energy Density	1.4 × 10^4 J m^{-3}

Table 3.1: Standard values for a 10 nm diameter magnetite (iron ferrite) nanocrystal. These values are used to compute the standard specific loss power q_0, approximately 440 mW g^{-1}.

literature, are listed in Table 3.1. We may then vary each parameter independently and compare them to a standard specific loss power, q_0, to determine what parameters increase the losses.

For the purpose of this model we assume that the relaxation time τ is dependent only upon the Néel relaxation time τ_N because the nanocrystals will be physically bound to the cell membrane. This forces the particles to remain stationary, prohibiting Brownian relaxation.

Transmitter Optimization

The transmitter has two parameters that may be controlled to optimize the loss power: the field frequency and amplitude. The normalized specific loss power (the $q(f, H_0)$ divided by q_0) is plotted against both field frequency and field amplitude for experimentally realizable values of both parameters in Figure 3-1.

Figure 3-1 demonstrates a monotonic increase with both field and amplitude. Simply put, higher frequencies and fields induce more loss per gram in our nanocrystals. Equation 3.16 would suggest that the specific loss power increases linearly with both frequency and field amplitude; however, Figure 3-1 suggests otherwise. This is because there is an non-explicit dependence on the frequency and amplitude through ξ. Figure 3-1 appears to suggest that the largest field-amplitude combination possible should produce the largest losses.

However, there exists a constraint on the amplitudes we can apply to an *in vivo* system. If the frequency and amplitude are too high, then eddy currents will be

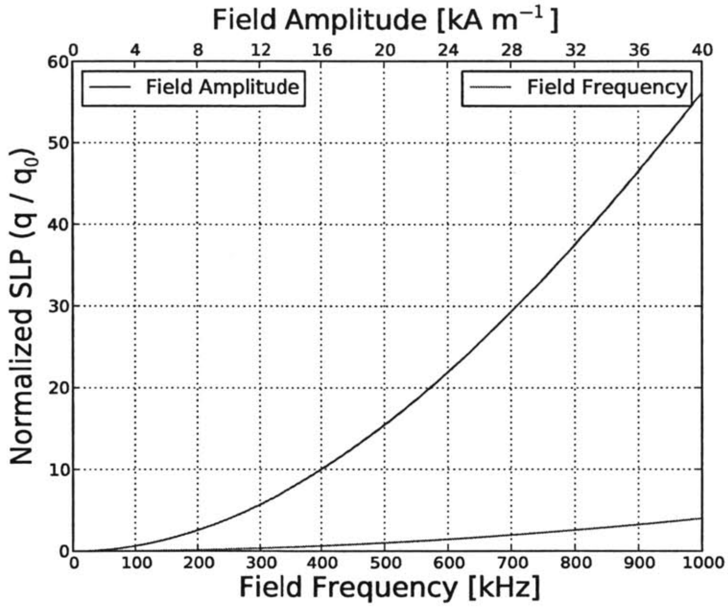

Figure 3-1: Normalized specific loss power versus field frequency and amplitude. The loss power increases monotonically with both field and amplitude.

induced in tissue, causing unintentional heating within the target. Brezovich experimentally studied this phenomenon, and developed the criterion that the product $f \times H_0$ must be less than 4.85×10^8 A m $^{-1}$ s^{-1} for a 30 cm diameter coil.[Bre88] Brezovich noted that patients subjected to magnetic fields of these levels "had a sensation of warmth, but was able to withstand the treatment for more than one hour without major discomfort".

From Faraday's Law, the current induced by a changing magnetic field is proportional to $f \times H_0 \times A$, where A is the area of the current loop. The loop's area is proportional to the square of its diameter d, so the induced current I is proportional to $f \times H_0 \times d^2$. The power dissipated P is proportional to I^2, so have the relationship:

$$P \propto (H_0 f d^2)^2 \tag{3.17}$$

In Section 5.2.1 we determined that the series capacitor C_S in our circuit determines its operating frequency. Thus we choose f as our independent variable; that is, f determines the field amplitude H_0. Rearranging Equation 3.17:

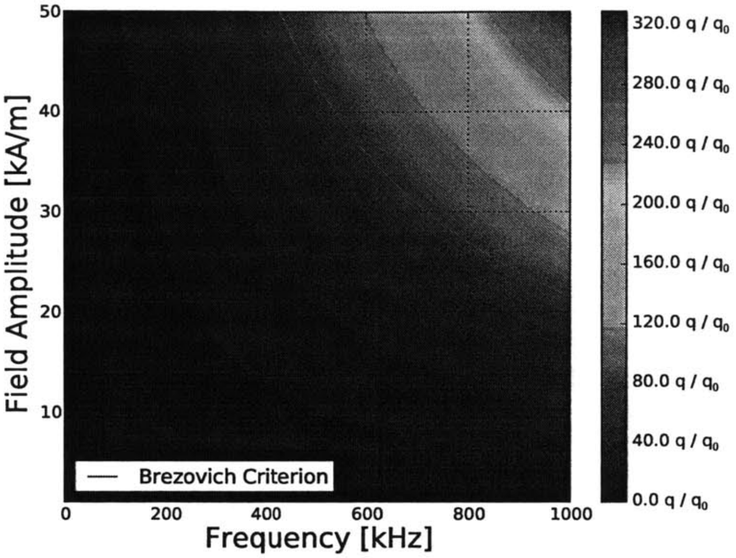

Figure 3-2: A two-dimensional contour map of the normalized specific loss power versus field frequency and amplitude. The Brezovich Criterion is shown in red delineating the maximum allowed field-amplitude product.

$$H_0 = \frac{\sqrt{P}}{f d^2} \tag{3.18}$$

If we set d to 30 cm, then $\frac{\sqrt{P}}{d^2} = 4.85 \times 10^8$ A m^{-1} s^{-1} and we get the original Brezovich Criterion back. This suggest can rewrite the Brezovich Criterion for any diameter coil as:

$$H_0 = \frac{4.85 \times 10^8}{f} \frac{d_0^2}{d^2} \tag{3.19}$$

where d_0 is 30 cm, and d is the diameter of the constructed coil. Equation 3.19 can be used to compute the maximum allowed field amplitude at a given frequency. Figure 3-2 shows a contour plot of q_0 versus field frequency and amplitude with the Brezovich Criterion overlaid.

Figure 3-2 shows that the specific loss power can be significantly increased by operating at the Brezovich Limit. The Brezovich Limit occurs at approximately 100 times the losses of our standard set of parameters. Figure 3-3 shows the normalized

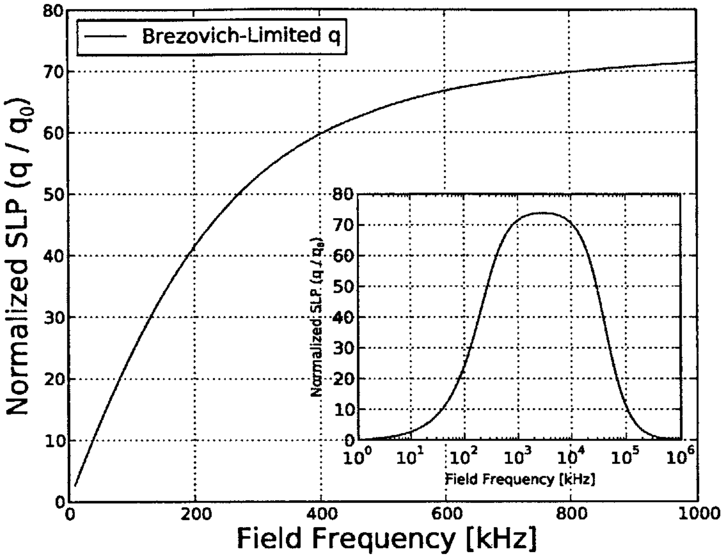

Figure 3-3: A plot of the normalized specific loss power at various frequency-amplitude pairs, as dictated by the Brezovich Criterion. The inset shows q/q_0 between 1 kHz and 1 GHz on a log-log plot, showing the broad peak centered around 3 MHz.

specific loss power at each point along the curve defined by the Brezovich Criterion.

Figure 3-3 shows that for frequencies below 1 MHz, the losses can be increased substantially by increasing the frequency and decreasing the field amplitude according to the Brezovich Criterion. However, this technique yields diminishing returns.

The inset shows that for frequencies above 1 MHz the loss power plateaus, reaching a maximum at approximately 2.9 MHz before declining again. Far beyond after approximately 10 MHz the specific loss power begins to drop off again, eventually returning near the baseline. The specific loss power thus exhibits a very broad (9 MHz) peak beginning at approximately 1 MHz; all values within this broad peak are within 5% of each other, suggesting that the system is not extremely sensitive to frequency. This broad peak suggests that there is some sort of frequency-dependent peak in the specific loss power. However, it must be noted that as the frequency approaches 1 GHz our model begins to break down; in the GHz range ferro- and ferrimagnetic resonance begins to dominate, which is absent in our model.

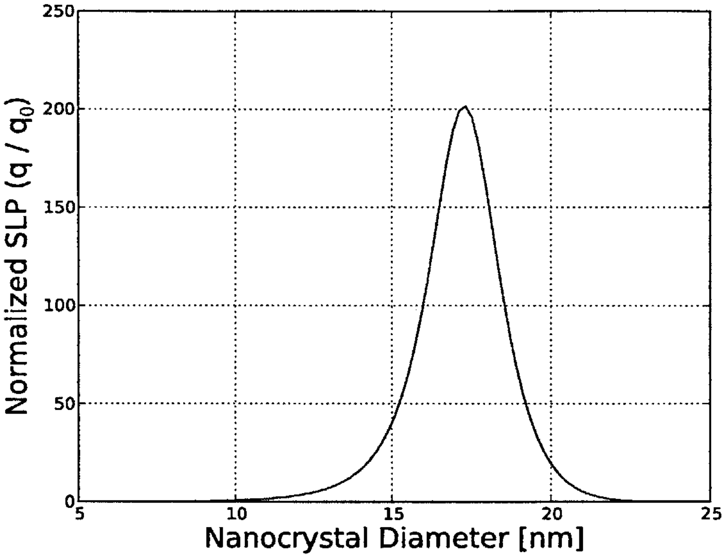

Figure 3-4: A plot of q/q_0 versus nanocrystal diameter. The optimum peak occurs at $d = 16.4$ nm

Nanocrystal Optimization

There are three parameters related to the nanocrystal that can be altered to increase q – the nanocrystal diameter, anisotropy energy density, and specific magnetization. The former is a function of the synthesis technique (related to the time allotted to the growth phase), while the latter two parameters are dictated by the chemical identity of the nanocrystal – the selection of M in MFe_2O_4. Figure 3-4 shows how the losses change as a function of the nanocrystal diameter d.

Figure 3-4 shows a clear peak at approximately 16.4 nm, where the specific loss power increases by over a factor of 170. However, the peak is very narrow – q is less than 50% of its peak value if the diameter is off by only 0.12 nm. This also demonstrates why monodispersity in the nanocrystal population is of utmost importance – with a standard deviation of ± 2 nm, as is common with aqueous coprecipitation methods, only about 4.8% of the nanocrystals will lie within the top half of the loss peak. With monodisperse populations, the majority of the nanocrystals will lie in the loss peak, greatly increasing the heating power of the ensemble.

To determine why the diameter has such a large and narrow peak, we must de-

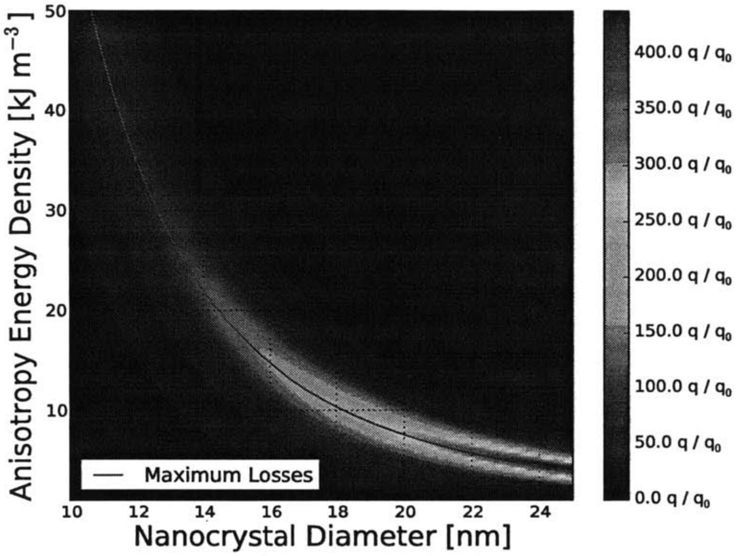

Figure 3-5: A contour plot showing how the specific loss power varies with anisotropy energy density and nanocrystal diameter. The curve of maximum losses indicates the prescence of an optimal KV product.

termine what role the volume, V plays in the specific loss power. It appears twice: once in the Néel relaxation time (Equation 3.10 in the KV product that determines the anisotropy energy of a nanocrystal, and again the ξ (Equation 3.15) where the product $\sigma\rho V$ determines the magnetic moment of the nanocrystal population. Figure ?? shows a contour map of the normalized q versus diameter and anisotropy energy density.

There is a clear curve of maximum losses moving from the top left of Figure 3-5 to the bottom right. This indicates the prescence of an optimal KV product – the anisotropy barrier. Figure ?? shows the curve of constant energy in red that gives the highest specific loss power. On this curve, the anisotropy energy barrier was numerically computed to be approximately $2.371 \pm 0.003 \times 10^{-20}$Joules. This anisotropy barrier produces a Néel relaxation time that is approximately equal to the drive frequency (for q_0, this is 500 kHz), maximizing the losses as described in Section 3.1.1.

We may then postulate that for a frequency f, there exists an optimal anisotropy energy KV that forces the Néel relaxation time to be equal to the time between peaks in the magnetic field. This would suggest that the optimal frequency to operate at is given by:

$$f = \frac{1}{2\pi\tau_0 e^{-\frac{-KV}{k_B T}}} \tag{3.20}$$

Equation 3.20 is valid when Néel relaxation is the only mechanism. More generally, $f = \frac{1}{2\pi\tau}$ for the relaxation time τ as defined in Equation 3.11. When the field frequency matches the relaxation frequency, we call such a system relaxation resonant. Figure 3-6 shows the specific loss power as a function of both the anisotropy energy and the field frequency. For a given anisotropy energy, there exists an optimal resonant frequency f that locally optimizes the specific loss power q. The red line shows this relaxation resonance peak for all anisotropy energies. As the resonance decreases in frequency, the maximum attainable q increases – this is due to the Brezovich Criterion, which allows a higher field amplitude at lower frequencies, increasing q.

Figure 3-6 also shows that as the diameter increases, the possible heating power that can be achieved increases. Besides the relaxation resonance effect, there exists a magnetic effect – as the diameter increases, the total magnetic moment (the product $\sigma\rho V$) of the fluid increases, increasing the losses.

Figure 3-7 shows the effect of varying the specific magnetization σ with the diameter on specific loss power. For any fixed diameter, increasing the specific magnetization increases the specific loss power. However, there is a trough where a relatively lower magnetization will produce the same specific loss power. This occurs at a diameter of 16.34 nm – the same peak that was found in Figure 3-4, where the anisotropy energy hits a critical value. This demonstrates two points:

1. There exists a critical anisotropy energy that produces the largest specific loss power by setting the Néel relaxation time equal to the drive frequency.

2. The specific magnetization can be increased indefinitely to improve the heating power.

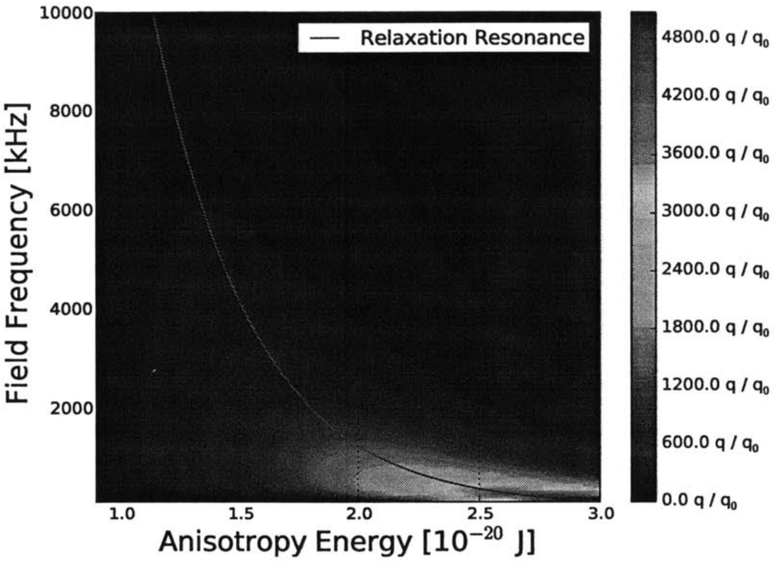

Figure 3-6: The relaxation resonant frequency as a function as anisotropy energy KV. For a given product KV there is a single broad peak. As frequency decreases, the Brezovich Criterion allows a higher amplitue to be used, increasing the maximum specific loss power.

This is demonstrated in Figure 3-8, where the specific loss power is shown as a function of diameter and specific magnetization at three different anisotropy energy densities. Shifting the anisotropy energy density moves the peak to a different diameter (to match the operating frequency), but in all cases increases the specific magnetization monotonically increases the loss power.

However, it must be noted that the anisotropy energy density and specific magnetization are not independent parameters, and thus cannot be tuned separately. According to Stoner-Wolfarth Theory, the work done per unit volume in changing the magnetization from 0 to a magnetization M is:[CG08]

$$W = \int_0^M H dM \tag{3.21}$$

The work done is simply the area between the magnetization curve and the M axis. If this amount of work is required to magnetize the sample, then the work must be equal the anisotropy energy stored in the material. If the sample's volume is

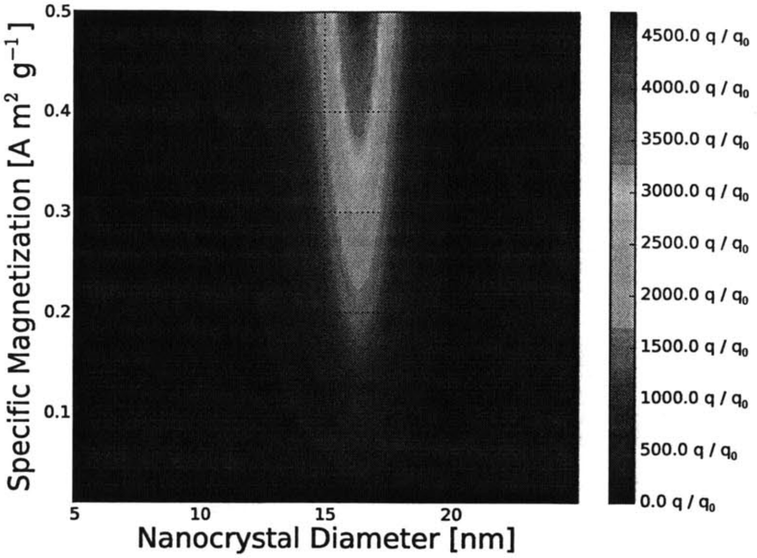

Figure 3-7: The magnetic effect of diameter increase on q. Larger diameters creates larger nanocrystal volumes, increasing the product $\sigma\rho V$, therefore increasing the heating power.

known, the anisotropy energy density K can be determined from this measurement.

While the relaxational losses are independent of hysteresis, hysteresis remains a point of much confusion in determining the anisotropy constant. The above method assumes no hysteresis in the sample; if hystereis is present, then when the field is returned to zero a remanent magnetization M_R will remain. In this case, the energy

$$E_R = \int_{M_R}^{M} HdM \tag{3.22}$$

is returned to the field, while the energy

$$E_S = \int_{0}^{M} HdM - \int_{M_R}^{M} HdM \tag{3.23}$$

is stored in the sample. When the field reverses and undergoes one full cycle, twice this energy will be dissipated as heat.

We have constrained our original five parameters into three free parameters, reducing our parameter space to a simpler one. Our free parameters are the field

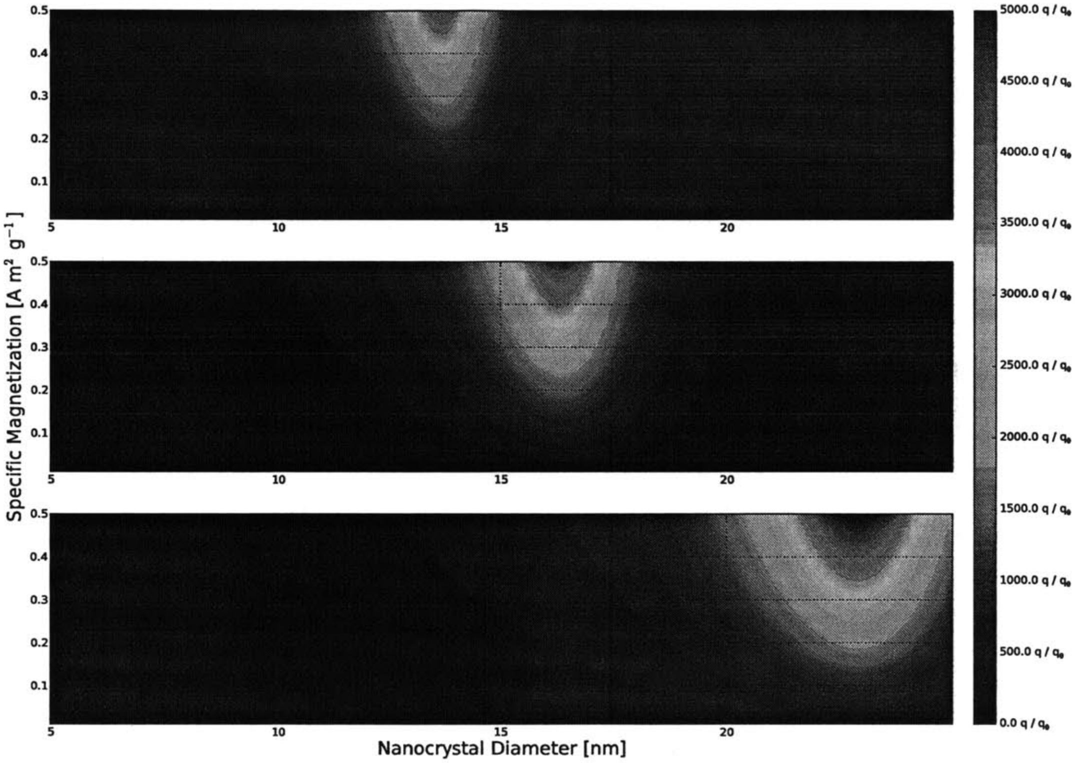

Figure 3-8: Specific loss power as a function of specific magnetization and diameter for three values of anisotropy energy density: 36 kJ m^{-3} (top), 12 kJ m^{-3} (middle), and 4 kJ m^{-3} (bottom). In each subsequent plot the relaxation resonance shifts; the peak SLP lies at the center of this relaxation resonant peak.

frequency f, the nanocrystal diameter d, and the material identity (encompassing K and σ). Once these three properties are chosen, the remainder of the parameters are determined. These criteria for optimizing the power transfer in our system are:

1. For a given material, identify its diameter and anisotropy energy.
2. Tune the frequency to the relaxation resonance using Equation 3.20.
3. The amplitude is determined by the Brezovich Criterion at a given frequency.

However, it is of note that when the relaxation resonant frequency can be made small (through large particle diameter or high anisotropy) it is ideal to do so in order to increase the maximum field amplitude. This is a novel approach in that we find a way to maximize q for a given nanocrystal structure and composition. Once the nanocrystal has been characterized, the optimal external field parameters are chosen. This, along with a variable-frequency transmitter, allows experiments to be run optimally with any nanocrystal chemistry, rather than the traditional method of tuning the chemistry to create the optimal q at a fixed field frequency and/or amplitude.

3.1.3 Materials Selection

In this section we study the effect of materials chemistry on q with two goals in mind:

1. Compute the relaxation resonance for various metal ferrite nanocrystals.
2. Determine if there exists an ideal chemistry for use in frequencies between 100 kHz and 10 MHz.

We use iron, nickel, manganese, and cobalt ferrite in our study. The relevant properties of each chemistry is listed in Table 3.2.

Figure 3-9 shows the computed q for a variety of metal ferrites. For each ferrite, the anisotropy energy density K and specific magnetization σ were held constant while the diameter and frequency were varied. The field amplitude H_0 was Brezovich-limited.

Chemistry	K (J m^{-3})[SISI87]	σ (A m^2 g^{-1})[CG08]
Fe_3O_4	1.4×10^4	0.092
$CoFe_2O_4$	1.8×10^5	0.080
$MnFe_2O_4$	3.3×10^3	0.080
$NiFe_2O_4$	3.3×10^3	0.050

Table 3.2: Material properties listed for four common metal ferrites. The specific magnetizations are listed for bulk ferrites, whereas the anisotropy energy density data is taken from measurements of coprecipitated nanocrystals.

By selecting a ferrite chemistry the parameter is reduced from five free parameters to only two, allowing a global maximum to be determined.

To maintain an optimal q, small diameter requires high frequencies and vice versa. This is because the relaxation resonance moves to higher frequencies for small diameter due to a smaller anisotropy barrier. The second observation is that lower frequencies and larger diameter induce the largest q. This is because of a combination of the Brezovich Criterion and the magnetic effect discussed earlier. At lower frequencies higher field amplitudes are reachable, and in turn larger diameters are used which also increases the total magnetic moment of the nanocrystal colloid. However, it must be noted that larger nanocrystals are more difficult to synthesize than small ones – as nanocrystals grow, their monodispersity decreases and the probability of a magnetic domain forming (and therefore making the particle ferromagnetic rather than superparamagnetic) increases. Therefore, we must balance the desires to keep the particle size low while simultaneously utilizing a lower frequency.

The data suggests that magnetite (iron ferrite) and manganese ferrite are the best choices for nanoscale receivers. This is due to their combination of high specific magnetization and a relaxation resonance at an attainable diameter. Cobalt ferrite's relaxation resonance peak is very narrow – less than half a nanometer – suggesting that synthesizing nanocrystals at this optimal size would be very difficult. If the nanocrystals were synthesized with a mean diameter even half a nanometer off of the peak, then their heating power would suffer substantially. For this reason cobalt ferrite is not a suitable candidate. Nickel ferrite offers the same relaxation resonance as manganese ferrite, however its specific magnetization is 62% that of manganese

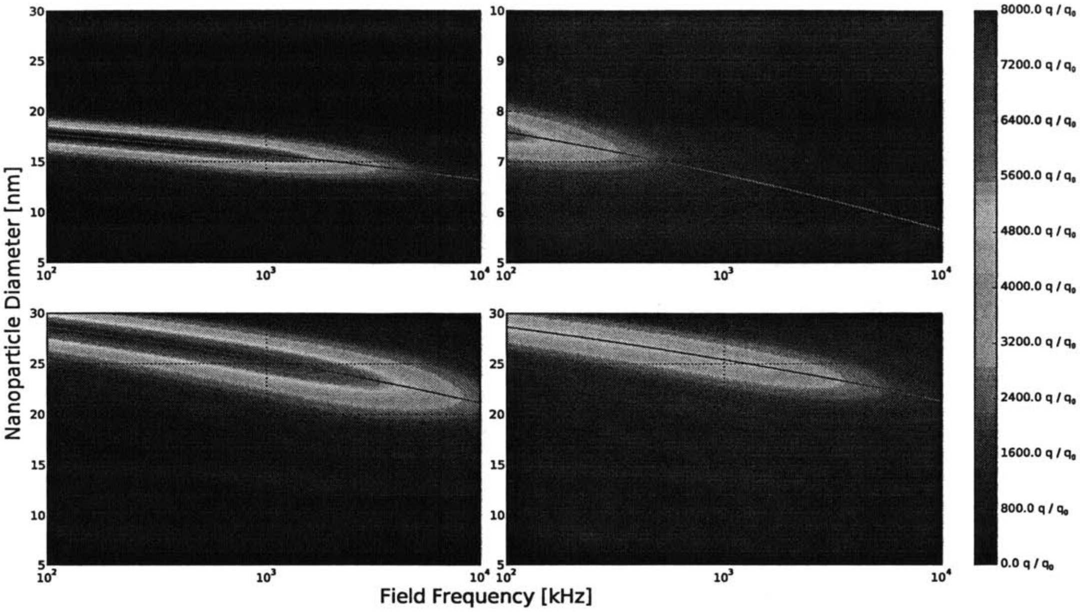

Figure 3-9: From top left to bottom right, the Specific Loss Power versus frequency and diameter for (a) iron ferrite (magnetite), (b) cobalt ferrite, (c) manganese ferrite, and (d) nickel ferrite. The red lines delineate the optimal diameter for each frequency. From this it is apparent that iron ferrite and manganese ferrite offer the largest heating power in the radiofrequency range.

ferrite, resulting is a significant decrease in heating power.

3.2 Summary

In this chapter we examined the theory of magnetic losses in ferrite nanocrystals. Through examining the theory of losses we deduced that there are five experimental parameters that can be controlled by the experiment – the external field's amplitude and frequency, and the nanocrystal's diameter, anisotropy energy density, and magnetization. Furthermore, we were able to reduce our parameter space by determining which parameters had coupled effects. It was found that the field amplitude is fully determined by the field frequency according to the Brezovich Criterion, and that the anisotropy energy density and nanocrystal diameter together set the relaxation time for the magnetic moment of the nanocrystal. This three-parameter space suggests that the optimal losses occur when the nanocrystal's relaxation time and the external field frequency match; the losses can further be optimized by increasing the specific magnetization of the nanocrystal and the external field amplitude.

Chapter 4

Nanocrystal Antennae

The last chapter outlined a suitable biological target for noninvasive neuronal stimulation. The next step is develop a method to stimulate this genetic target by producing heat *in vivo*. The field of oncology has exploited hyperthermia therapy for cancer treatment since the 1950s[GMS+57]; in this treatment ("magnetic hyperthermia") the radiofrequency losses in magnetic nanocrystals is used to initiate necrosis in tumors. We use a modified version of this technique where a small amount of heat generation (causing an increase in temperature on the order of 3-5 ° rather than full necrosis is required. In order to generate heat in tissue, two components are necessary: a nanocrystal receivers and an excitation source. The first portion of this thesis will focus on the optimization of magnetic nanocrystals as nanoscale radiofrequency receivers.

Aqueous colloids of nanocrystals have become increasingly common in biotechnology. Such systems have found a variety of applications, including MRI contrast agents[LHJ+07], remote drug release[DvH+07], protein purification[MPGP07], and magnetic hyperthermia[HDMZ06]. Colloidal nanocrystals are ideal for such tasks because of their nanoscale diameters and subsequent magnetic behavior. Nanoscale crystals are substantially smaller than typical cells (whose diameter is typically 1-5 μm) and much closer to the size of proteins, allowing for precise biological targeting. In addition, their small scale allows for simple delivery to a biological target. The small size of such nanocrystals physically limits the number of magnetic domains that can form; for a small enough nanocrystal the entire crystal behaves as a single magnetic moment. These single-domain nanocrystals behave as paramagnets due to the thermal relaxation of their magnetic moments (as phenomena known as superparamagnetism); they are easily magnetizable in the presence of a field but have a small remanent magnetization and coercivity, which prevents flocculation in solution.

4.1 Synthesis

There are a variety of methods available that are suitable for synthesizing a monodisperse population of magnetic nanocrystals.[LFP⁺08] The simplest and most efficient synthesis is the chemical coprecipitation of iron salts, developed by Massart.[Mas81] Metal ferrite nanocrystals are prepared by the alkalinization of a stoichiometric mixture of a ferric salt (such as $FeCl_3$) and the salt of a divalent metal M (such as Fe_2SO_4, $Co(NO_3)_2$):

$$M^{2+} + 2Fe^{3+} + 8OH^- \rightarrow MFe_2O_4 + 4\ H_2O \tag{4.1}$$

This technique produces a large quantity of nanocrystals with size ranging from single nanometers[BPS⁺90] to microns[SENJ⁺08]. The primary advantage of this technique is its simplicity – it can be performed under standard ambient temperature and pressure conditions and the product precipitates rapidly from solution. However, control over particle size and dispersity is extremely coarse in this method. This is because of an overlap of the nucleation and growth phases of crystal growth – critical cluster sizes form due to local supersaturation, nuclei begin to grow, and then diffusion of the dissolved ions to the nuclei surface limits the growth rate. A more ideal synthesis would not rely on local supersaturation to begin nucleation, instead maintaining clear nucleation and growth phases such that all nuclei form and growth simultaneously.

One such alternate approach to synthesis is high-temperature decomposition of iron organic precursors (such as $Fe(CO)_5$ or $Fe(acac)_3$[1] in organic solvents. In such a

---

[1] acac = acetylacetonate

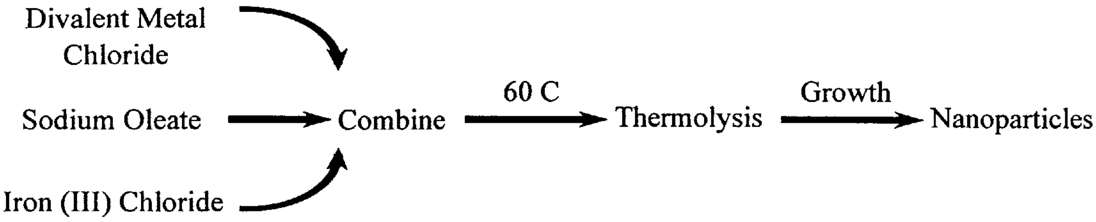

Figure 4-1: A flowchart illustrating the synthesis of metal ferrite nanocrystals using thermolysis of a mixed-metal precursor.

synthesis, the organic precursor is decomposed at high temperatures in the presence of a surfactant (such as oleic acid, to stabilize the colloid) and then aged for a variable period of time to control the size.[SZR+03] The separation of the decomposition and nucleation phase from the growth phase allows for a very fine control of final nanocrystal diameter. The size and the morphology can be controlled by varying the reaction times and temperature, but the organic solvent used, concentration of reactants, precursors, and surfactants each play a significant role in determining the final structure.[SLM09]

We use a synthesis method based off the one published by Bao et. al[BSA+09], modified to increase the yield. This synthesis occurs in two steps – the formation of an organometallic (metal-oleate) precursor, and then the thermolysis of the precursor to form nanocrystals. A graphical overview of the process is shown in Figure 4-1. The mixed metal-oleate complex is formed through the reaction of sodium oleate with a stoichiometric ratio of metal and iron chlorides. Sodium oleate and metal chlorides are mixed together in a solution of water, ethanol, and hexane and subsequently refluxed at 60 °C for 4 hours. The resulting mixed-metal complex ($M\mathrm{Fe}_2$-$(\mathrm{C}_{18}\mathrm{H}_{33}\mathrm{O}_2)_4$) was allowed to cool to room temperature before isolation. Isolation was performed by removing the aqueous phase (bottom layer) and then evaporating the remaining ethanol and hexane at 70 °C for 30 minutes and the remaining water at 100 °C for 60 minutes. This synthesis is summarized in Table 4.1.

After the precursor has been formed, 5 grams of the mixed-metal oleate precursor is combined with 0.5 g of oleic acid and 20 mL of 1-octadecene in a three-neck round bottom flask. The flask is evacuated for 15 minutes and then placed under flowing

Reactant	Amount
$FeCl_3$	20 mmol
MCl_2	10 mmol
Sodium Oleate ($C_{18}H_{33}O_2Na$)	80 mmol
H_2O	50 mL
Ethanol	50 mL
Hexane	100 mL

Table 4.1: The mixed-metal oleate precursor is formed through the reflux of the above reactants at 60 °C for 4 hours.

Reactant	Amount
Mixed-Metal Oleate Precursor	5 g
1-octadecene	20 mL
Oleic acid	0.5 g

Table 4.2: The mixed-metal precursor is mixed with oleic acid and 1-octadecene and then heated to 310 °C for thermolysis.

nitrogen. The mixture is then heated to 310 °C at a rate of 100 °C/hr and then held at 310 °C for one hour. The flask is then removed from the heat source and allowed to cool to room temperature. Bao et. al suggest from alternating gradient magnometry measurements that between 250 and 300 °C the mixed-metal oleate complex begins to dissociate into metallic cations and the oleate anion; at approximately 300 ° the critical concentration is achieved and homogeneous nucleation occurs in the solution.[BSA+09] The nucleation process is complete within approximately one minute, upon which the concentration drops below the nucleation threshold and the growth processing begins.

Once cooled, the oleate-stabilized nanocrystals are easily soluble in hexane.

4.2 Stabilization

It is imperative that synthesized nanocrystals are able to be stably dispersed into an aqueous phase for biological applications. While dispersed in a liquid, the colloidal stability of the magnetic nanocrystals is dependent upon four primary factors:[BPS+90]

1. electrostatic repulsion from surface charges

2. van der Waals attraction between nanocrystals
3. magnetic dipole-dipole interactions
4. steric repulsion due to the presence of surfactants

The sum of these four forces must be carefully balanced to prevent aggregation of the nanocrystals while in solution.

Iron atoms on the surface of magnetite nanocrystals coordinate with hydroxyl groups in the aqueous phase, leaving the surface hydroxylated.[BPS+90] These amphoteric hydroxyl groups may react with acids or bases to produce a positive or negative surface charge; however, at physiological pH (approximately 7.4), the isoelectric point is reached and the surface charge drops to zero. At this point brownian motion and van der Waals attraction causes flocculation of the nanocrystals occurs, necessitating the tuning of electrostatic and steric forces to stabilize the particles in solution.

The two common routes to stabilization is via the use of either monomeric stabilizers or polymer coatings. Monomeric stabilizers (such as citric acid, dimercaptosuccinic acid (DMSA), or gluconic acid) are typically acids that readily dissociate in the aqueous phase. The anions then bind to the nanocrystal surface and stabilize the particle via electrostatic repulsion.[LFP+08] The primary advantage of monomeric stabilizers is their small size – large polymeric stabilizers can increase the hydrodynamic diameter of nanocrystals and restrict their access to confined spaces *in vivo*. In contrast, polymeric stabilizers (such as dextran, polyethylene glycol (PEG), or polyvinyl alcohol (PVA)) dramatically increase the hydrodynamic radius (often by as much as 10 or 15 nm) but serve as stronger stabilizers due to multiple hydrogen bonding domains along their length.[TMVV+06] Polymeric stabilizers also possess a high level of variation in polymers allows for extensive bioconjugation options by changing functional groups on the polymers, rather than requiring the selection of a new stabilizer.

Magnetic nanocrystals synthesized using our technique will be stabilized with oleic acid, allowing for solubility in nonpolar solvents such as toluene or hexane.[SZR+03]

In order to exchange the surfactant to allow for transfer to the aqueous phase, we perform a ligand exchange. The first step is to remove excess oleic acid through centrifugation and discarding of the supernatant. A mixture of 1 part ethanol to 3 parts hexane was added to the nanocrystal colloid in a 50 mL centrifuge tube, and subsequently cetrifuged at 6000 rpm for 10 minutes. The supernatant was discarded, leaving precipitated nanocrystals in the centrifuge tube. The nanocrystals were resuspended in 10 mL of hexane by vortexing, and 10 mL of ethanol were added to the solution. The solution was again centrifuged at 6000 rpm for 10 minutes, the supernatant discarded, and resuspended in 10 mL hexane. A glass vial was massed, and the nanocrystal solution was added to the vial. The hexane was evaporated at 100 °C and the vial was again massed to determine the mass of nanocrystals.

To exchange the ligand, 10 mg of nanocrystals suspended in hexane were added to a glass vial. The nanocrystals were vacuum distilled to remove the solvent, and then resuspended in 2 mL of tetrahydrofuran (THF). 20 mg of poly(ethylene glycol)-derivatized phosphine oxide (PO-PEG) was then added to the solution and vortexed to dissolve. The solution was then vacuum distilled again to remove the THF, leaving the stabilized nanocrystals, and then heated to 150 °C for 1 hour while still under vacuum. After the mixture was cooled to room temperature, an aqueous colloid was formed by adding 5 mL of water and vortexing to dissolve the stabilized nanocrystals. The solution was then filtered using a 220 nm syringe filter to remove any aggregates.

4.3 Characterization

The above synthesis method was used to synthesize three common metal ferrites: cobalt, manganese, and nickel ferrite. These are three of the most well-studied ferrites (after iron ferrite, also known as magnetite). These ferrites are also very simple in that the divalent metal must be present in a 2:1 ratio with the trivalent iron ion; this is in contrast to more complex ferrites such as manganese-zinc ferrite ($Mn_xZn_{1-x}Fe_2O_4$) or strontium ferrite ($SrFe_{12}O_{19}$).

Transmission electron microscopy was utilized to investigate the size distribution

Chemistry	d (nm)
Ni	25
Mn	12
Co	12

Table 4.3: Three total samples were synthesized and stabilized using the process described above. Their diameters as determined by TEM are listed.

resulting from the synthesis. TEM samples were prepared by mixing 1 μL of 10 mg mL^{-1} nanocrystal solution (dissolved in hexane) with 200 μL of hexane and adding 10 μL of the dilution to an amorphous carbon-coated copper grid. The hexane was allowed to dry, depositing the nanocrystals on the grid. The grid was then cleaned by placing the grid on laboratory tissue, dropping 10 μL of methanol onto the grid, and allowing the grid to dry. This was repeated a total of three times to clean the grid. The samples were subsequently imaged using a JEOL 200CX General Purpose TEM (200 kV).

Figure 4-2 shows a representative image taken via TEM. This image illustrates that the synthesis produces a highly monodisperse ($\frac{\delta d}{d} \approx 10\%$) population of spherical nanocrystals with a finely controlled size. Table 4.3 shows a full table of the samples that were synthesized, the final solvent (particles in water were stabilized using PEG, while particles in toluene remained stabilized by oleic acid), and the diameter as determined by TEM.

4.4 Summary

This chapter presented a flexible method for the synthesis of aqueous phase monodisperse metal ferrite nanocrystals. The proposed chemistry is extremely flexible, allowing for the synthesis of varying composition and diameter nanocrystals. In addition, a stabilization protocol is demonstrated that allows the synthesis nanocrystals to be suspended in the aqueous phase for extended periods of time. This is ideal for *in vivo* applications, where the nanocrystals will need to be subjected to physiological conditions without aggregation or flocculation. The synthesized nanocrystals were then subsequently characterized using transmission electron microscopy to demonstrate

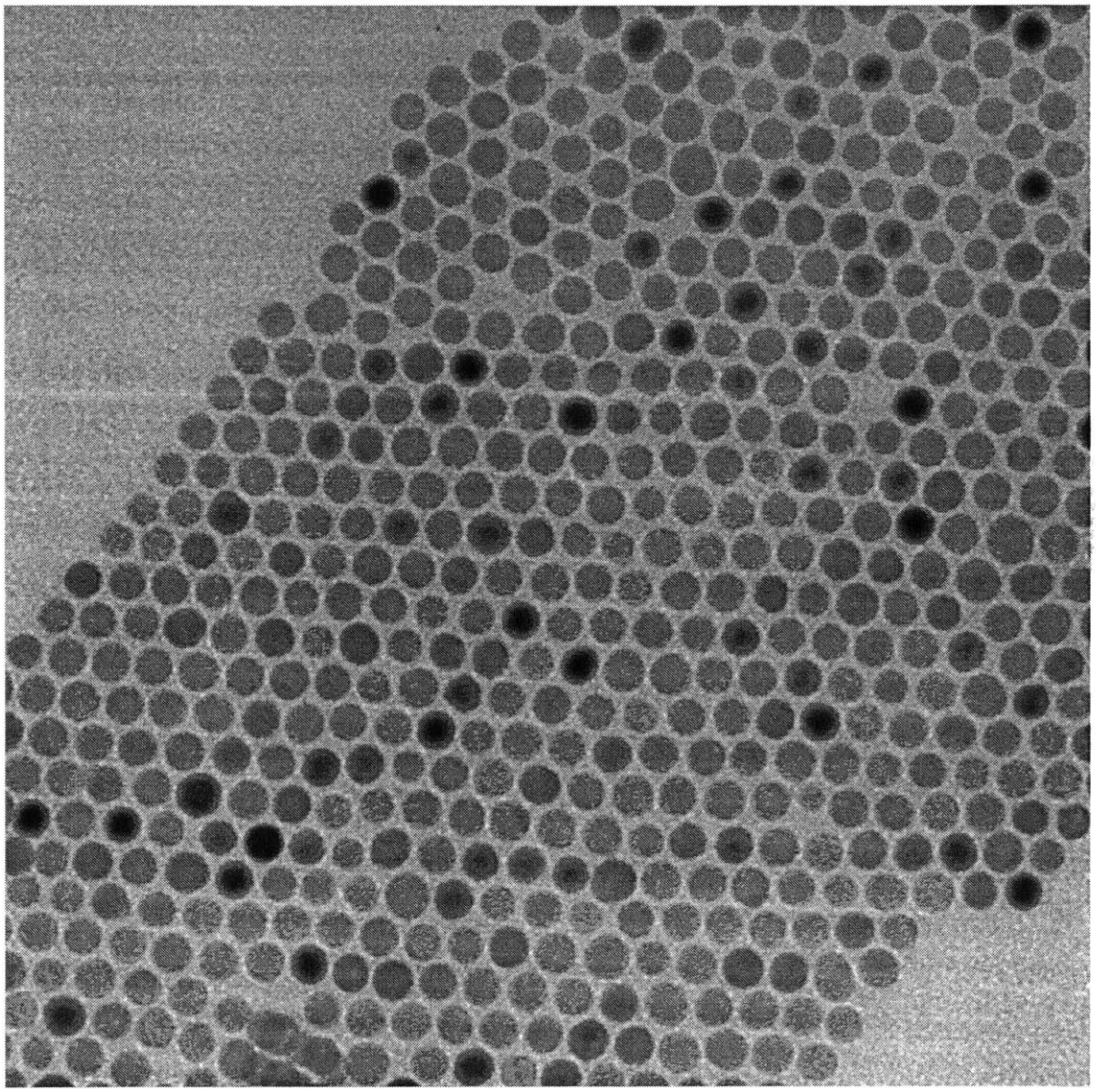

Figure 4-2: A representative TEM image of the synthesized nanocrystals. The synthesis produces highly monodisperse spherical nanocrystals.

the size control.

Chapter 5

Radiofrequency Transmitter

The last two chapters focused primarily on the design and synthesis of colloidal nanocrystals to serve as nanoscale radio receivers; now our attention turns to the design and construction of a suitable excitation source. The excitation source must be simple and cost-effective to construct while being capable to provide moderate magnetic fields (up to 30 kA m^{-1}) at low radiofrequencies. This chapter describes the theory and implementation of such an excitation source.

5.1 Design

Solenoids are useful for producing large uniform magnetic fields ranging from a few A m^{-1} to 16000 kA m^{-1}. A typical solenoid is constructed from many turns of insulated copper wire wound around a tube of electrically insulating, low-permeability material (to reduce its effects on the generated magnetic field). For a solenoid with inner diameter d and length l, the field H (in kA m^{-1} at an axial distance x from the center of the solenoid is given by

$$H = \frac{NI}{10l}\left[\frac{l+2x}{2\sqrt{d^2+(l+2x)^2}} + \frac{l-2x}{2\sqrt{d^2+(l-2x)^2}}\right] \tag{5.1}$$

where N is the number of turns and I is the current flowing through the solenoid. At the center of the solenoid ($x = 0$), the maximum field is given by

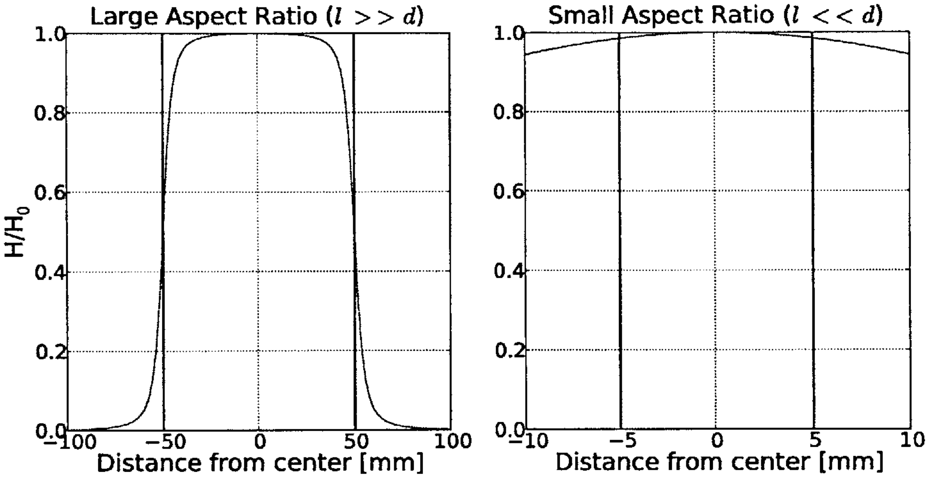

Figure 5-1: The influence of aspect ratio on the uniformity and divergence of the magnetic field H. The left images shows a large aspect ratio (black lines indicates the edges of the solenoid) and the right image shows a small aspect ratio.

$$H = \frac{NI}{10l}\left[\frac{l}{\sqrt{d^2+l^2}}\right] \tag{5.2}$$

Equation 5.2 suggests that the two critical ratios for solenoid construction is the turn ratio ($\frac{N}{l}$) and the aspect ratio ($\frac{l}{d}$). For fixed solenoid dimensions, increasing the turn ratio (through packing turns more tightly or winding multiple layers of wires) is the most desirable form of increasing the field. This is because the ohmic losses in the wire increase as I^2R for a resistance R; thus an increase in total wire length linearly increases the ohmic losses whereas an increase in current quadratically increases in the losses for the same gain in H.

The aspect ratio determines the uniformity of the field. For a solenoid with a large aspect ratio ($l >> d$), the magnetic field inside the solenoid is very uniform over the middle half. However, the field at the edges of the solenoid are only half of the field at the center. In contrast, for a small aspect ratio ($d >> l$), the field is not uniform inside the solenoid, but the field at the edges of the solenoid may be as little as 10% less than the field at the center. Thus, the aspect ratio embodies the tradeoff between a high field outside of the solenoid and uniformity inside the solenoid's length. Figure 5-1 demonstrates this tradeoff.

The above considerations give rise to the following design criteria:

- The diameter d of the solenoid is determined primarily by the space required for the sample.
- The aspect ratio is selected to provide the requisite field uniformity for the sample.
- For given d and l, the turn ratio is required by the field required given the current that can reasonably be supplied by the power supply.

The electrical impedance (Z) of a circuit element is a measure of how much the element opposes the flow of current. It can be separated into two components – the resistance (R) is the real component of the impedance and represents the dissipative behavior of the element; the reactance X is the imaginary component and represents the induction and storage of energy in the element. To achieve maximum power transfer from a source to a load, the source impedance (Z_S) must equal the complex conjugate of the load impedance (Z_L):

$$\begin{aligned} Z_S &= Z_L && (5.3) \\ R_S + iX_S &= R_L - iX_L && (5.4) \end{aligned}$$

That is, the impedances must sum to zero and the resistances must match. This can be accomplished through the use of a matching network (to match reactances) and transformers (to match resistances).

A solenoid is typically defined by its inductance L. However, most inductors (especially hand-wound ones) are extremely non-ideal; for this reason we include in our model the resistance of the wire comprising the solenoid (R_L), and the self-capacitance of the solenoid windings (C_L). These three elements can be combined into the lumped element model shown in Figure 5-2 with an impedance given by Equation 5.5.

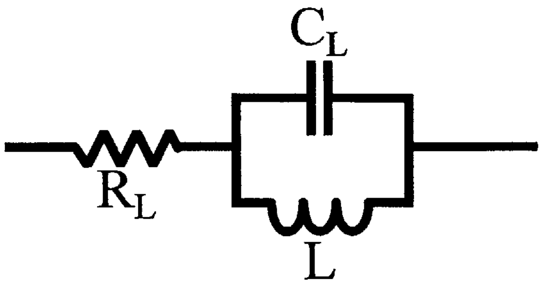

Figure 5-2: A lumped element model for a solenoid. The solenoid is characterized by its inductance L, self-capacitance C_L, and resistance R_L.

$$Z_L = R_L + \frac{i\omega L}{1 - LC_L\omega^2} \tag{5.5}$$

It is apparent that the inductor possesses a self-resonant frequency $\omega_L = \frac{1}{\sqrt{LC_L}}$ at which the denominator disappears. Below this self-resonant frequency, the denominator increases, subsequently decreasing the solenoid's impedance. This allows more current to flow, allowing a larger magnetic field to be generated. On the other hand, above the self resonant frequency the impedance increases dramatically, impeding the flow of current and attenuating the magnetic field. This suggests that our solenoid operates most efficient when our operating frequency ω is below the self-resonant frequency ω_L.

As described in Section 5.1, the power transfer between an alternating current source and its load (the solenoid) is maximized when the load impedance is equal to the complex conjugate of the source impedance. For many sources of alternating current signals, the source impedance is required to be 50 Ω; therefore, to meet our power transfer criteria the solenoid must be combined with an impedance matching network to bring its overall impedance to 50 Ω.

If a capacitor C_s is added in series with the solenoid, the impedance of the network becomes:

$$Z_{\text{Network}} = R_L + \frac{i\omega L}{1 - LC_L\omega^2} - \frac{i}{\omega C_s} \tag{5.6}$$

It can be observed from Equation 5.6 that the addition of a series capacitor can

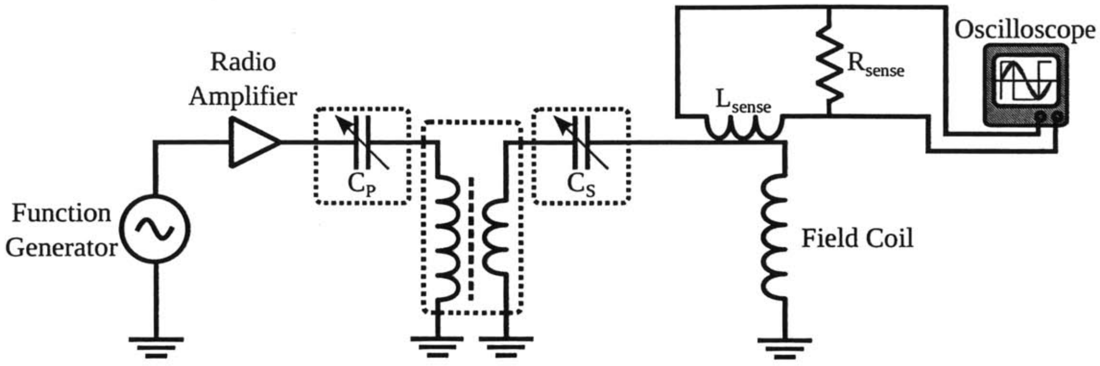

Figure 5-3: Schematic of the final impedance matching network. Shielded enclosures are shown with dotted lines.

completely eliminate the network's reactance if the capacitor value is selected to be equal to

$$C_s = \frac{1 - \frac{\omega^2}{\omega_L^2}}{L\omega^2} = \frac{1 - LC_L\omega^2}{L\omega^2} \tag{5.7}$$

This leaves only the real component of the impedance R_L. This remaining component of the impedance can be matched to 50 Ω by utilizing a transformer. For a transformer with N_P turns on the primary coil and N_S on the secondary coil, the impedance of the solenoid network Z_L will appear to be

$$Z_{\text{Network}} = \frac{N_P^2}{N_S^2} R_L \tag{5.8}$$

By choosing the appropriate number of turns on the primary and secondary coil, the solenoid network can perfectly match the source impedance $Z_S = 50\Omega$, maximizing the power transfer. However, the addition of a transformer also adds the reactance $i\omega L_P$, where L_P is the inductance of the primary coil of the transformer. To remove this reactance, a capacitor C_P is added in series with the transformer, following the logic above.

It is also important to be able to characterize the magnetic field produced by our solenoid. The magnetic field may be calculated theoretically by Ampère's Law given that we know the current through the solenoid. While a properly tuned impedance matching network should allow 100% power transfer, in reality various losses make that value much less. Therefore we constructed a current probe to measure the current through the solenoid. The current probe is a transformer with a single turn on the solenoid's side that induces current in the secondary coils (L_{sense} in Figure 5-3). The current is then read as a voltage across a 50 Ω resistor (R_{sense} in Figure 5-3) with an oscilloscope or digital multimeter. The current through the secondary (I_{sense}) can then be determined by Ohm's Law and the field is computed as

$$H = \frac{N_{Field} N_S I_{sense}}{l} \tag{5.9}$$

where N_{Field} is the number of turns on the field-producing coil and N_S is the number of turns on the secondary coil.

A function generator is used to set the input frequency in conjunction with a radiofrequency power amplifier to provide the high voltage and current necessary to create large magnetic fields.

In summary, the criteria for optimizing the performance of a solenoid are:

- Construct the solenoid such that $\omega < \omega_0$.
- Select a value for the series capacitor C_s such that the reactance is minimized.
- Construct a resonant transformer with appropriate turns ratio to transform the network resistance to 50 Ω, with a series capacitor C_P selected to match the resonant frequency of the transformer and the solenoid.

5.2 Construction of Excitation Sources

5.2.1 In Vitro Coil

With a firm understanding of the design considerations, a solenoid may be constructed to stimulate the synthesized nanoantennae. The first step is to determine the size of our sample, as outlined above. For *in vitro* samples, it is convenient to use a petri dish to hold cell cultures. In addition, it is necessary to maintain optical access to

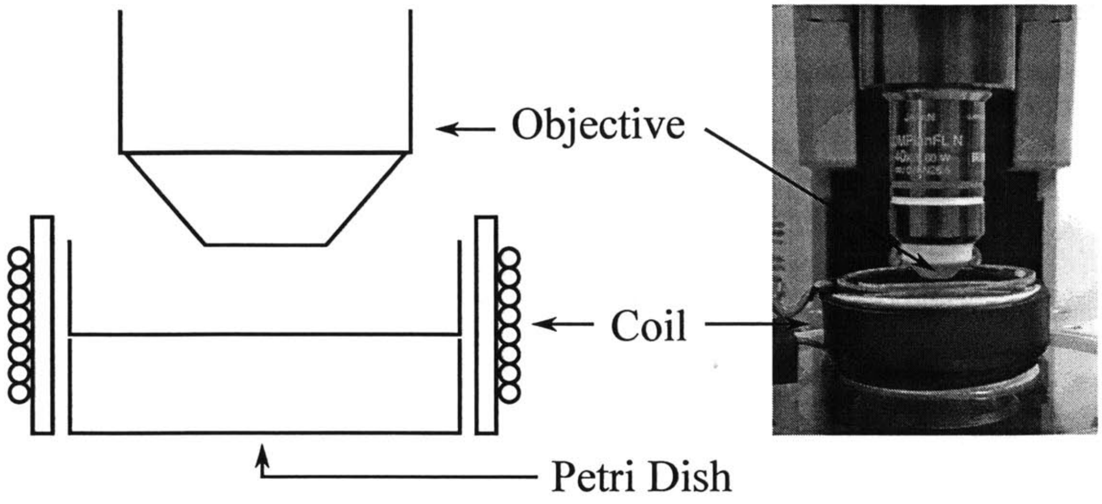

Figure 5-4: Left: Design of the in vitro coil with a microscope objective for scale. Right: Photograph of the constructed in vitro coil. The solenoid has 8 turns around a 45 mm OD borosilicate scaffold. The sample sits on top of a petri dish to lift it into the center of the magnetic field.

the sample so that fluorescence techniques can be used to monitor the sample. Electrophysiology measurements also require the placement of electrodes in the sample, necessitating a low aspect ratio so that the electrodes may reach the sample. However, the sample is planar, allowing for a non-uniform field within the solenoid.

The chosen petri dishes are 40 mm in diameter; thus, we choose 45 mm OD borosilicate glass tubing as a core to wind our solenoids around. Borosilicate glass was chosen for its low magnetic permeability and low thermal expansion coefficient in addition to its affordability. The core is cut to be 20.6 mm tall with a Buehler 11-1190 low speed saw with a diamond blade to a height a 20 mm such that a microscope objective and electrophysiology electrodes may access the sample.

At radiofrequencies, standard copper wires have dramatically increased impedance due to the skin and proximity effects. To mediate these problems, Litz wire is traditionally used. A standard litz wire construction consists of many high-gauge copper wires individually insulated and woven together in a fashion that exposes each conductor to the outermost insulation for equal lengths. For our transmitter, we used a custom-wound Litz wire from HM Wire International (Ohio). Each wire contained 105 strands of 36 AWG copper wire woven into 5 bundles of 21 conductors, coated in a nylon outer insulation. Eight turns of Litz wire was wrapped around the outer diameter of the glass, using double-sided tape to hold the wires in place. After the appropriate number of turns were added, the wire was cut and polyolefin heatshrink was applied to hold the construction together. A female BNC connector was soldered onto the ends of the Litz wire and heatshrink was applied to the leads.

The current probe was constructed using magnetic wire around a ferrite core. A single turn from the field solenoid served as the primary, with 37 turns as the secondary. The number of turns on the secondary was limited only by the size of the ferrite. A 10x attenuator was used for measuring the sense current at fields of over 23 kA m^{-1}.

The type of dielectric chosen for the series capacitors must be able to withstand high currents and maintain low losses at high frequencies. Polypropylene capacitors were chosen for their low losses and resistance to stray eddy currents (to reduce heating). To allow for quick swapping of capacitors to test samples at multiple frequencies, the capacitors were placed in aluminum enclosures with mounted BNC connectors, as shown in figure 5-5.

The series capacitors serve to determine the operational frequency of the field coil. Our frequency spectrum was controlled by two constraints: first, the effective distance of radiofrequencies through human tissue is at least 10 cm between 100 kHz and 50 MHz[Ros87]; second, our radiofrequency amplifier was rated for up to 15 MHz. Therefore we seek to operate between 100 kHz and 15 MHz. The series capacitor value was computed to force the benchtop coil to resonate at intervals of 100 kHz, and capacitors were purchased that were as close to the computed values as reasonably possible. The benchtop coil was used for frequency-dependent testing, and once an ideal operating frequency was chosen (see Chapter ??) C_s and C_p were chosen for the in vitro coil.

To determine the ideal operating frequency, it is convenient to construct a coil that can characterize the heating power of nanocrystals in solution. For that purpose we construct a magnetic susceptometer using these same principles.

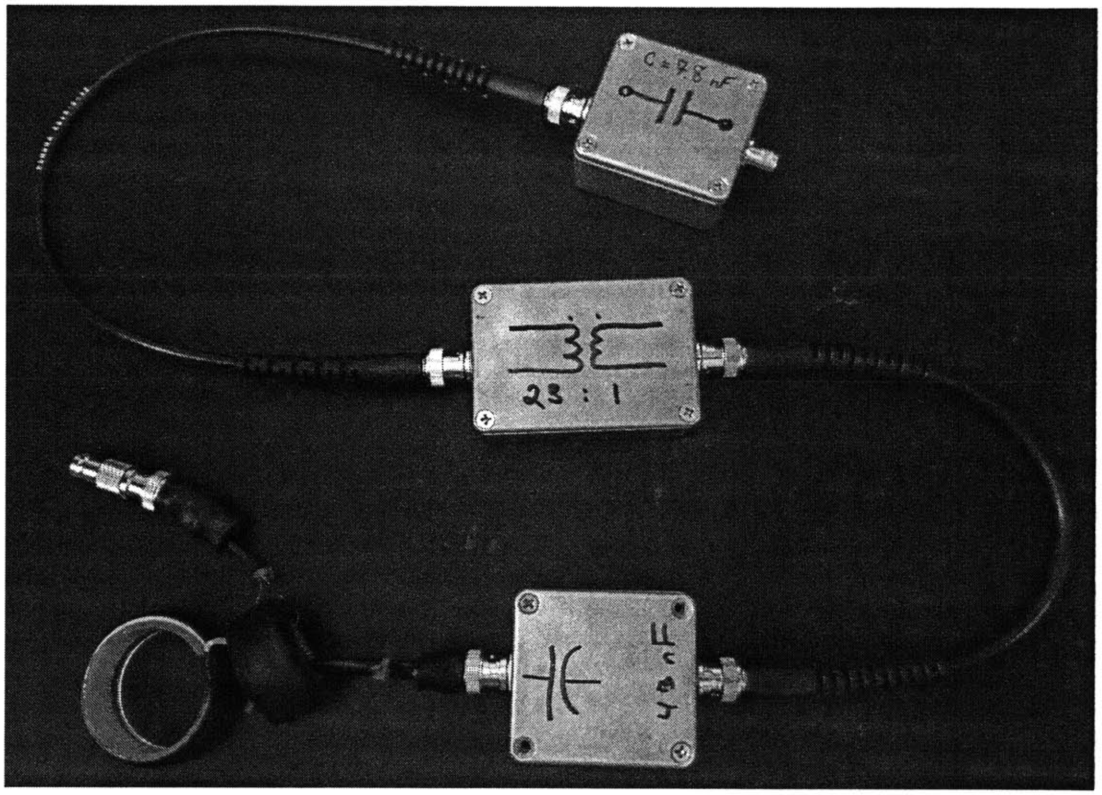

Figure 5-5: The in vitro coil with completed impedance matching network. From top right to bottom left, following the cables: the primary capacitor C_P, the impedance-matching transformer, series capacitor C_S, current probe (unconnected), and the in vitro coil.

5.2.2 Susceptometer

The quantity of interest for our synthesized nanocrystals is their specific loss power. It would be ideal to measure their heating power calorimetrically; however, it is very difficult to measure increases in temperature with high precision and accuracy in the presence of an alternating magnetic field. Metal and semiconductor-based sensors such as thermocouples and thermistors are susceptable to self-heating due to induced eddy currents, resulting in drifting temperature readings. Non-magnetic thermometers (such as liquid-in-glass thermometers) add a large thermal mass to the sample and are extremely slow with poor precision. Optical pyrometers avoid many of these downsides but have low sensitivity in the temperature regime near body temperature. Optical fiber thermometers that utilize infrared light to measure the temperature can make extremely fast and precise measurements; however, these thermometers require a controller and the entire system is prohibitively expensive.

Direct measurements of the magnetic losses avoids many of the drawbacks of calorimetric measurements. As noted in Equation 3.7, the specific loss power is directly proportional to the quadrature susceptability χ''; therefore, if we can measure χ'' the relative specific loss power of synthesized nanocrystals can be measured.

A schematic of a typical susceptometer is shown in Figure 5-6. A function generator is used to drive a solenoid (L_P) that serves as the primary coil in an air-core transformer. Two identical coils, L_{Search} and L_{Ref}, are connected in series with opposing polarities to make a differential measurement. The primary coil creates a magnetic field H that induces a current I_S in the secondary coils. If the two coils are geometrically identical, they will each have an equal current induced in them and therefore an equal induced electromotive force. Connecting them in reverse series ensures that the combined voltage as detected at the output is zero.

If a magnetic sample is placed inside of the search coil, then the search coil experiences a magnetic flux equal to:

$$B = \mu_0(1 + \chi)H \tag{5.10}$$

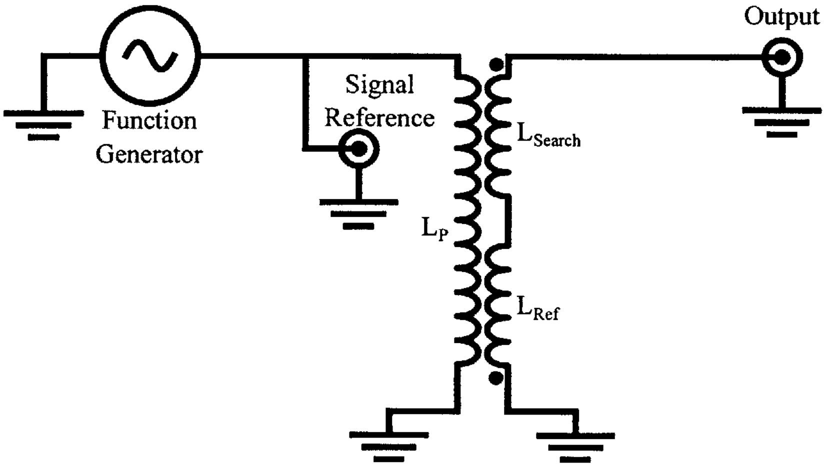

Figure 5-6: A schematic of the magnetic susceptometer used to measure the magnetic losses in colloidal nanocrystal solutions.

where as the reference coil experiences a flux equal to simply $\mu_0 H$. Thus the total electromotive force detected at the output is only dependent upon $\mu_0 \chi H$.

The susceptometer is constructed from 100 turns of Litz wire around a core of 16 mm OD borosilicate glass that is 195 mm long to ensure a uniform field for the sample. The search and reference coils are constructed from 20 turns of Litz wire, placed a quarter of the coil length from each end of the coil. The sample is placed in a glass ampule that may hold up to 200 μL of colloidal solution; the glass ampule fits into the primary coil to hold the sample in the center of the search coil. For relative quantification of specific loss powers, high magnetic fields and optimal power transmission are not necessary, so we ony use a single monolayer of turns and omit the impedance matching network in our construction. An illustration of the susceptometer construction is shown in Figure 5-7

The quadrature susceptability is typically very small compared to the in-phase susceptability; therefore the use of a lock-in amplifier is required. A typical lock-in amplifier is shown in Figure 5-8.

A lock-in amplifier operates on the principle of phase-sensitive detection. A signal source provides an AC signal $V_{source}\cos(\omega t)$ that is used to excite our system of interest. The output signal of the system is typically an attenuated and phase-shifted signal $V_{sys}\cos(\omega t+\phi_S)$. The output of the system is first amplified by a preamplifier to

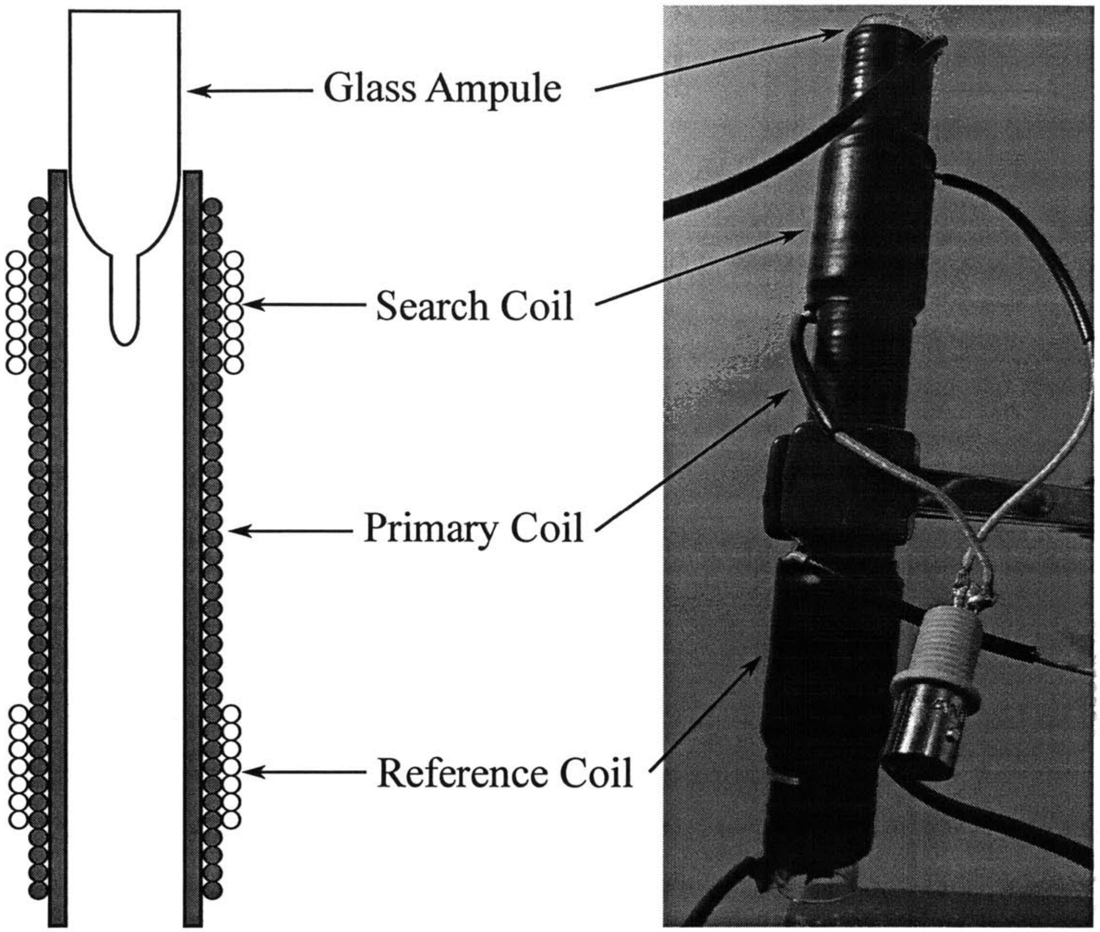

Figure 5-7: Left: A schematic of the susceptometer coil with the primary coil construction shown in grey, and the secondary coils in white. Right: A photograph of the constructed susceptometer.

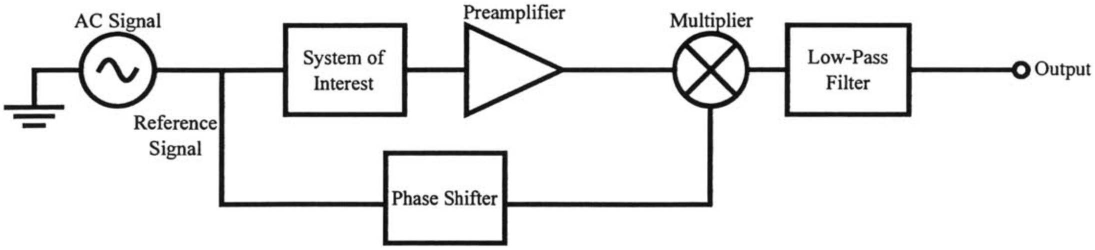

Figure 5-8: A block diagram showing how a typical lock-in amplifier operates.

increase the size of the signal, and then multiplied by a reference signal $V_{ref}\cos(\omega t + \phi_R)$. The output of the multiplier V_M is given by:

$$V_M = V_{sys}\cos(\omega t + \phi_S) \cdot V_{ref}\cos(\omega t + \phi_R) \tag{5.11}$$

$$V_M = \frac{V_{sys}V_{ref}}{2}\left[\cos(\phi_S - \phi_R) + \cos(2\omega t + \phi_S + \phi_R)\right] \tag{5.12}$$

Equation 5.12 shows that there are two components of the resultant signal: a DC component at zero frequency and a component at the frequency 2ω. If a low pass filter is used with a cut-off frequency less than 2ω, only the DC component is seen in the output.

By considering Equation 3.4 and Equation 5.10 simultaneously, it is apparent that the system output is equal to:

$$V_{output} = \mu_0 H_0\left[(1+\chi')\cos(\omega t + \phi_S) + \chi''\sin(\omega t + \phi_S)\right] \tag{5.13}$$

where ϕ_S is the phase acquired from the system. If this is substituted into Equation 5.12 then the locked-in signal is given by:

$$V_{lock-in} = \frac{\mu_0 H_0 V_{source}}{2}\left[(1+\chi')\cos(\phi_S - \phi_R) + \chi''\sin(\phi_S - \phi_R)\right] \tag{5.14}$$

where we assume that the reference signal is the same frequency as the system output. If the reference signal is set the same phase as the system-acquired phase ϕ_S, then the output of the lock-in is simply the in-phase component; if the reference phase is offset by $\frac{\pi}{2}$, then the lock-in outputs the quadrature component.

Measurement of the quadrature can be simplified by two facts: the impedance of an ideal solenoid is purely reactive (implying that there is no dissipation) and that the magnitude of the signal vector (R) of the quadrature (Y) and the in-phase component (X) must remain constant at:

$$R = \sqrt{X^2 + Y^2} \tag{5.15}$$

Thus the quadrature component can be found with knowledge of just the in-phase component and the total magnitude of the signal vector. The magnitude of the signal vector can be found by measuring the locked-in signal of the susceptometer with no sample; because there are only reactive (energy-storing) components to the impedance, the magnitude and in-phase component are equal:

$$R = \sqrt{X_0^2} \tag{5.16}$$

Equation 5.12 tells us that the output signal is at a maximum when the reference phase is equal to the output signal's phase. With the reference phase set, the magnetic sample can be introduced to the susceptometer, introducing a quadrature component Y. Combining Equations 5.15 and 5.16, the quadrature component can be found by:

$$Y = \sqrt{X^2 - X_0^2} \tag{5.17}$$

The implementation of our lock-in amplifier is shown in Figure 5-9 with component values given in Table 5.1. The TLC071 was chosen as our operational amplifier of choice for its relatively high gain-bandwidth product (10 MHz) and cost-effectiveness. The preamplifier supplies a gain of 5 to the search coil's output; then signal then proceeds to the AD835 4-Quadrant Multiplier which serves to demodulate the signal with a reference. The phase shifter is implemented as an active all-pass filter with unity gain and phase shift determined by the pull-down resistor R_5. The phase can be shifted between 180 and 0 degrees by manually setting the value of the 1 kΩ potentiometer. The output of the multiplier is then conditioned by an active low-pass filter with a cut-off frequency set to 3.38 Hz that removes the doubled frequency components, leaving only the component of the signal that is in-phase with the reference. The active filter also provides a gain of 10 to amplify the final signal, to improve the precision of the measurement. The split-supply was created from a DC power supply and a resistive divider, shown in the upper right corner of Figure 5-9.

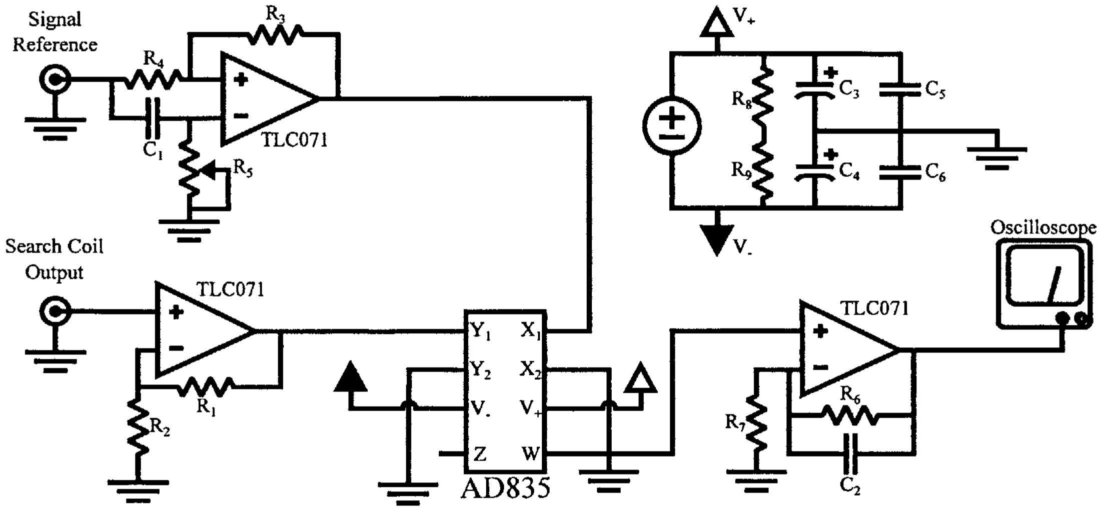

Figure 5-9: A schematic of the lock-in amplifier used to determine the quadrature susceptability. Not shown: each integrated circuit has a 0.01 μF bypass capacitor between the positive and negative supply pins (V_+ and V_-, respectively) and a 2.2 μF bypass between V_+ and V_-.

Resistor	Value	Capacitor	Value
R_1	1 kΩ	C_1	1.0 nF
R_2	3.9 kΩ	C_2	0.47 μF
R_3	1 kΩ	C_3	100 μF
R_4	1 kΩ	C_4	100 μF
R_5	1 kΩ	C_5	0.1 μF
R_6	1 kΩ	C_6	0.1 μF
R_7	10 kΩ		

Table 5.1: Component values for the lock-in amplifier shown in Figure 5-9. Not listed are the bypass capacitor values.

5.3 Characterization

The frequency response of each coil was fully characterized using Bode plots. The voltage output of the coil was taken to be the current probe for the in vitro coil, and the search coil for the susceptometer coil. Each Bode plot was taken by sweeping the input frequency between 10 kHz and 10 MHz with an output voltage of 5 V$_{pp}$ and measuring the response at the output.

The Bode plot for the susceptometer is shown in Figure 5-10. The susceptometer exhibited a self-resonance near 6 MHz; as per our criteria, this is above our desired

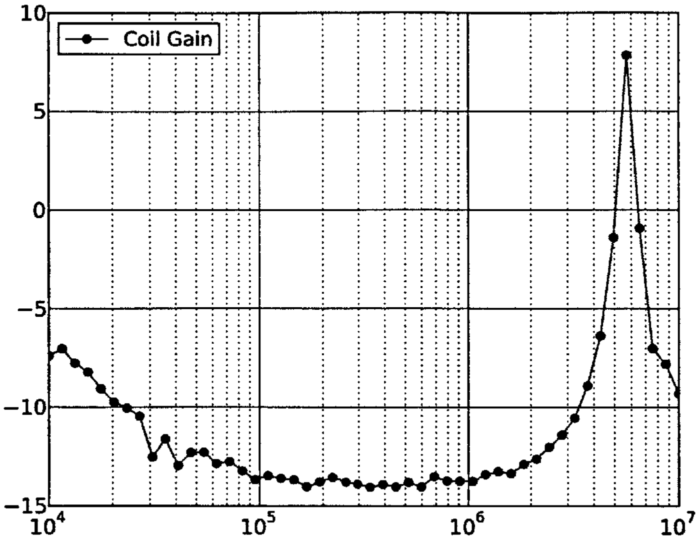

Figure 5-10: A Bode plot demonstrating the frequency response of the susceptometer primary coil with respect to the search coil. Note the flatband response between 100 kHz and 1 MHz. Solid lines are to guide the eye.

operating range. In addition, the susceptometer's primary coil exhibited a flatband frequency response between 100 kHz and 1 MHz, making the matter of changing operating frequencies extremely straightforward.

The inductance of the in vitro coil was found to be 6 μH using an LCR Meter. Using this value of inductance, ten capacitor values were chosen to set the resonant frequency at 10 evenly distributed points between 100 kHz and 1 MHz. Due to the discrete nature of available capacitors, the closest available values were used. The actual values used and resulting resonant frequencies are shown in Table 5.2. The Bode plots in Figure 5-11 show that the addition of a series capacitor creates a clear resonance at the desired frequency, and that variation of the series capacitor shifts the resonant frequency as described earlier in this chapter.

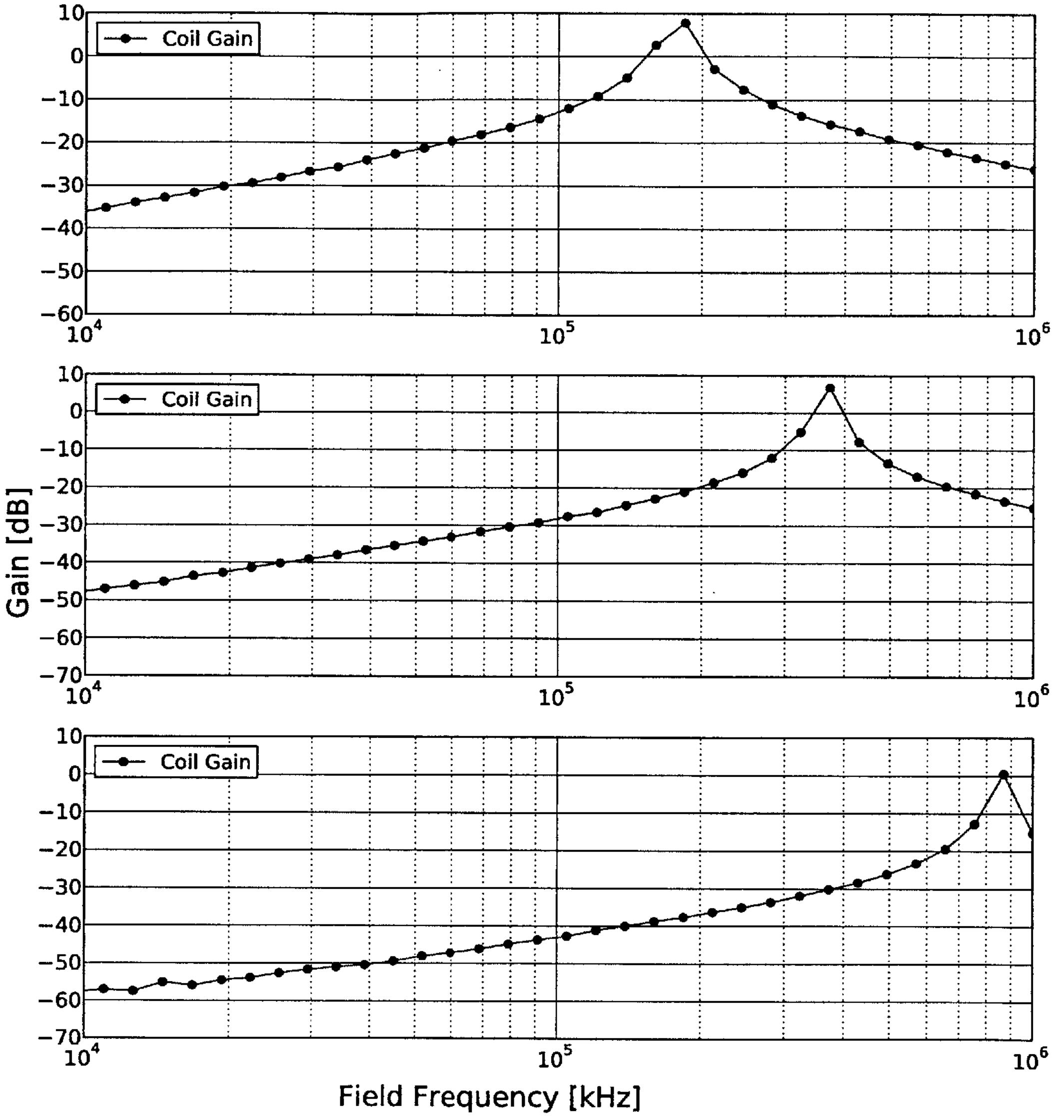

Figure 5-11: A Bode plot demonstrating the frequency response of the *in vitro* coil with a series capacitance of 470 nF (top), 43 nF (middle), and 4.7 nF (bottom). Solid lines are to guide the eye.

Frequency (kHz)	Theoretical C_s (nF)	Actual C_s (nF)	Actual Frequency (kHz)
100	422 nF	470 nF	94.7
200	105 nF	91 nF	215
300	46.9 nF	43 nF	313
400	26.4 nF	22 nF	438
500	16.8 nF	16 nF	513
600	11.7 nF	12 nF	593
700	8.62 nF	8.2 nF	717
800	6.59 nF	6.8 nF	787
900	5.21 nF	5.6 nF	868
1000	4.22 nF	4.7 nF	947

Table 5.2: Capacitor values chosen to reach 10 frequencies between 100 kHz and 1 MHz. The actual value of C_s was chosen to be as close as possible to the computed value.

5.4 Summary

This section outlined the theory of designing a radiofrequency excitation source for the purpose of exciting magnetic nanocrystals. The theoretical and practical aspects of solenoid design were covered, and two solenoids were constructed using the described techniques – one suitable for *in vitro* experiments and one suitable for the characterization of nanocrystals in colloidal suspension. In addition, the design and implementation of a lock-in amplifier for use in characterizing the nanocrystal losses was documented. With a suitable excitation source constructed, it is now possible to measure the loss properties of the magnetic nanocrystals in comparison with the results of Chapter 3.

Chapter 6

Measurement of Magnetic Losses in Metal Ferrite Nanocrystals

The previous several chapters described a methodology for choosing optimal operating parameters for radiofrequency heating of nanocrystals, and then constructing the parts necessary to implement such a system. This chapter culminates that work in directly measuring the magnetic losses in synthesized nanocrystals.

6.1 Measurements

For each magnetic measurement, 200 μL of colloidal nanocrystals were placed in a glass ampule which was then loaded into the susceptometer. An oscilloscope was used to compare the reference phase and the susceptometer signal as described in Section 5.2.2. The phase difference was set to 90 degrees by varying the resistance of a potentiometer in the reference circuit, and was confirmed by ensuring that the signal was minimized when no sample was present in the susceptometer (representing a susceptometer signal that is entirely in phase). The operating parameters of the primary coil were then varied and the output signal was recorded.

Three synthesized nanocrystal samples were measured. Their properties are listed in Table 6.1, along with their computed Nèel relaxation frequency f_N. The results of Chapter 3 suggest that the optimal losses occur when our excitation source's frequency

Chemistry	d (nm)	K (kJ m^{-3}	f_N (MHz)
Ni	25	3.3	1.16
Mn	12	3.3	92
Co	12	180	20 μHz

Table 6.1: A table of the samples tested with the susceptometer, along with their computed relaxation resonant frequency (assuming only Nèel relaxation).

is matched to the relaxation time; unfortunately, the relaxation time of all of our particles is far outside of the attainable range for our system.

However, despite the lack of a reachable relaxation frequency, there are still trends that can be experimentally verified. The easiest one is the influence of frequency and amplitude on specific loss power. Figure 3-1 shows that the amplitude should have a much stronger effect on the loss power than the field frequency. This effect was measured by varying the amplitude of the primary coil's input sinusoid between 1 and 10 V_{pp} with a fixed field frequency of 500 kHz, and varying the field frequency between 100 kHz and 1 MHz with a fixed amplitude of 1 V_{pp}.

6.2 Results

The results are shown in Figure 6-1 for manganese ferrite. Comparing with Figure 3-1, the results are qualitatively very similar. Across nearly a decade of frequency and amplitudes, the frequency-dependence provides an increase only one tenth the increase seen via amplitude alone.

6.3 Summary

This chapter demonstrated the functionality of a homemade susceptometer for measuring the quadrature susceptability of colloidal nanocrystals suitable for *in vivo* radiofrequency heating. The nanocrystals were shown to qualitatively match the behavior expected based upon the theory described in Chapter 3, though no local maxima was observed due to the lack of an attainable relaxation frequency.

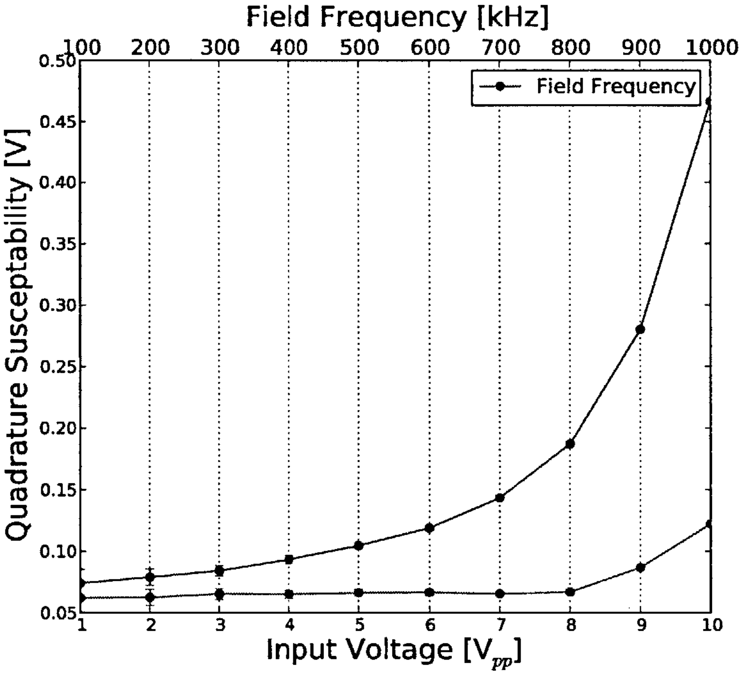

Figure 6-1: The measured quadrature susceptability for $MnFe_2O_4$ colloidal nanocrystals. Note that the amplitude dependence is much stronger than the frequency dependence.

Chapter 7

Conclusions

7.1 Summary

This manuscript sought to lay down initial groundwork for the radiofrequency stimulation of neurons. Previous work has shown that such stimulation is possible utilizing magnetic nanocrystals are nanoscale radio transducers; however, the demonstrated system responded several orders of magnitude slower than the target ion channel's kinetics and thus was far too slow for useful probing of neuronal ensembles. This thesis sought to carefully look at all of the components of this remote stimulation system and determine where optimizations could be made to improve the responsiveness of the system.

7.1.1 Nanocrystal Optimization

The first component that was examined were the superparamagnetic nanoparticles utilized as radiofrequency transducers. The theory of superparamagnetic losses was described in detail, determining five parameters that could be tuned to optimize the specific loss power. By looking at the relationships between these five parameters, the five-parameter space was reduced to a three-parameter space: the nanocrystal diameter, specific magnetization, and magnetic field frequency completely defined the specific loss power.

Modeling the magnetic losses led to an important insight regarding the design of an optimal remote heating system: because optimal heating occurs when the relaxation time of the nanocrystal matches the excitation frequency of the external field, the same increase in specific loss power can be achieved through either changing material properties or field parameters. This allows us to take the difficult problem of precise tuning of material parameters and transform it into a much simpler problem of tuning our excitation source.

A synthesis method for fine size control of monodisperse nanocrystals was developed based off of thermolysis of a mixed metal oleate precursor. This synthesis method allows us to synthesize nanocrystals with an accurate size distribution based off of our modeled results. An aqueous phase stabilization protocol was also developed to render the nanocrystals water soluble for *in vivo* applications.

7.1.2 Excitation Source

In addition to designing optimal nanocrystals, a variable-frequency, variable-amplitude excitation source was designed to allow for tuning of the field parameters to properly match those of the targetted nanocrystals. The design utilizes a single coil that is optimized for the sample geometry, with the frequency varied through the use of polypropylene capacitors. The design is simple to construct and made from easily attainable parts, eliminating the need for expensive induction furnaces. The design is also efficient enough that it does not require water cooling for moderate use.

7.1.3 Susceptometer

The final component of the thesis was the development of a susceptometer for directly measuring the magnetic losses (and therefore the specific loss power) of magnetic nanocrystals while suspended in colloidal solution. The design allowed for rapid *in vitro* testing of synthesized nanocrystals, allowing their behavior to be easily compared to theory. As a part of this design, a low-cost lock-in amplifier was constructed to allow for phase-sensitive detection of the quadrature component of the susceptability.

The susceptometer was then utilized to make magnetic susceptometry measurements on synthesized nanocrystals. Unfortunately our synthesized nanocrystals did not exhibit a relaxation frequency that fell within the tunable range for our excitation source; however, we were able to confirm the frequency- and amplitude-dependence of the susceptability.

7.2 Future Work

There are many directions that work derived from this thesis may take. A short-term goal would consist of making a series of more complete susceptometry measurements. A sample matrix of nanocrystals possession relaxation frequencies that were attainable with our susceptometer would provide an ideal set to perform further measurements on. Such a matrix could be used to further confirm or deny the theory described in Chapter 3.

A more long-term direction would be to take an optimized nanocrystal-radiofrequency transmitter system and implement the two *in vitro* to remotely stimulate cells. As demonstrated in the work of Huang et. al, remainder of the implementation presents a relatively straightforward problem in biology.[HDZ$^+$10] The stabilized nanocrystals may be conjugated with streptavidin and the target cells may be genetically tagged to express a biotinylated transmembrane peptide to serve as an anchor for the nanoscale receivers.[HT08] The targetted cells must either endogenously express TRPV1 or may be further treated to express the protein exogenously. Upon excitation with a radiofrequency source, the cell's status may be monitored via the use of calcium indicators (to monitor the activity of the TRPV1 channels directly) or electrophysiology techniques to record the action potential across the membrane.

If such the proposed system could be demonstrated with activation kinetics on the order of milliseconds or tens of milliseconds, radiofrequency stimulation could prove to be an extremely useful technique for studying the functions of neuronal networks.

Bibliography

[BK78] D Bentley and M Konishi. Neural control of behavior. *Annual Review of Neuroscience*, 1(1):35–59, 1978.

[BPS+90] Jean-Claude Bacri, Rgine Perzynski, Dominique Salin, Valrie Cabuil, and Ren Massart. Ionic ferrofluids: A crossing of chemistry and physics. *Journal of Magnetism and Magnetic Materials*, 85(13):27–32, April 1990.

[Bre88] I.A. Brezovich. Low frequency hyperthermia. *Medical Physics Monograph*, 16:82–111, 1988.

[Bro63] William Fuller Brown. Thermal fluctuations of a single-domain particle. *Physical Review*, 130(5):1677–1686, June 1963.

[BSA+09] Ningzhong Bao, Liming Shen, Wei An, Prahallad Padhan, C. Heath Turner, and Arunava Gupta. Formation mechanism and shape control of monodisperse magnetic CoFe2O4 nanocrystals. *Chemistry of Materials*, 21(14):3458–3468, July 2009.

[BZB+05] Edward S Boyden, Feng Zhang, Ernst Bamberg, Georg Nagel, and Karl Deisseroth. Millisecond-timescale, genetically targeted optical control of neural activity. *Nat Neurosci*, 8(9):1263–1268, 2005.

[CG08] B. D. Cullity and C. D. Graham. *Introduction to Magnetic Materials.* Wiley-IEEE Press, 2 edition, December 2008.

[CGC10] Paul Cherukuri, Evan S. Glazer, and Steven A. Curley. Targeted hyperthermia using metal nanoparticles. *Advanced drug delivery reviews*, 62(3):339–345, March 2010. PMID: 19909777 PMCID: PMC2827640.

[CK08] James J. Chambers and Richard H. Kramer. Light-activated ion channels for remote control of neural activity. *Methods in cell biology*, 90:217–232, 2008. PMID: 19195553 PMCID: PMC2788493.

[Cla03] David E. Clapham. TRP channels as cellular sensors. *Nature*, 426(6966):517–524, December 2003.

[Cri99] F Crick. The impact of molecular biology on neuroscience. *Philosophical Transactions of the Royal Society B: Biological Sciences*, 354(1392):2021–2025, December 1999. PMID: 10670022 PMCID: PMC1692710.

[CST+97] Michael J. Caterina, Mark A. Schumacher, Makoto Tominaga, Tobias A. Rosen, Jon D. Levine, and David Julius. The capsaicin receptor: a heat-activated ion channel in the pain pathway. *Nature*, 389(6653):816–824, October 1997.

[DHK71] M. J. Dennis, A. J. Harris, and S. W. Kuffler. Synaptic transmission and its duplication by focally applied acetylcholine in parasympathetic neurons in the heart of the frog. *Proceedings of the Royal Society of London. Series B. Biological Sciences*, 177(1049):509–539, April 1971.

[DvH+07] A. M Derfus, G. vonMaltzahn, T. J Harris, T. Duza, K. S Vecchio, E. Ruoslahti, and S. N Bhatia. Remotely triggered release from magnetic nanoparticles. *Advanced Materials*, 19(22):3932–3936, November 2007.

[FG83] I. C. Farber and A. Grinvald. Identification of presynaptic neurons by laser photostimulation. *Science*, 222(4627):1025–1027, December 1983.

[Gal91] Luigi Galvani. *De viribus electricitatis in motu musculari commentarius.* Accademia delle Scienze, Bologna, 1791.

[GCOZ97] Dwayne W Godwin, Diping Che, Donald M O'Malley, and Qiang Zhou. Photostimulation with caged neurotransmitters using fiber optic lightguides. *Journal of Neuroscience Methods*, 73(1):91–106, April 1997.

[GFM95] M. Glogauer, J. Ferrier, and C. A. McCulloch. Magnetic fields applied to collagen-coated ferric oxide beads induce stretch-activated ca2+ flux in fibroblasts. *American Journal of Physiology - Cell Physiology*, 269(5):C1093–C1104, November 1995.

[Gil05] Philip L. Gildenberg. Evolution of neuromodulation. *Stereotactic and Functional Neurosurgery*, 83(2-3):71–79, 2005.

[GMS$^+$57] R. K. Gilchrist, Richard Medal, William D. Shorey, Russell C. Hanselman, John C. Parrott, and C. Bruce Taylor. Selective inductive heating of lymph nodes. *Annals of Surgery*, 146(4):596–606, October 1957. PMID: 13470751 PMCID: PMC1450524.

[GR86] O.P. Gandhi and A. Riazi. Absorption of millimeter waves by human beings and its biological implications. *IEEE Transactions on Microwave Theory and Techniques*, 34(2):228 – 235, February 1986.

[HAd$^+$98] R. Hergt, W. Andra, C.G. d'Ambly, I. Hilger, W.A. Kaiser, U. Richter, and H.-G. Schmidt. Physical limits of hyperthermia using magnetite fine particles. *Magnetics, IEEE Transactions on*, 34(5):3745 –3754, September 1998.

[HDMZ06] Rudolf Hergt, Silvio Dutz, Robert Mller, and Matthias Zeisberger. Magnetic particle hyperthermia: nanoparticle magnetism and materials development for cancer therapy. *Journal of Physics: Condensed Matter*, 18(38):S2919–S2934, September 2006.

[HDZ$^+$10] Heng Huang, Savas Delikanli, Hao Zeng, Denise M. Ferkey, and Arnd Pralle. Remote control of ion channels and neurons through magnetic-field heating of nanoparticles. *Nat Nano*, 5(8):602–606, 2010.

[HHK52] A. L. Hodgkin, A. F. Huxley, and B. Katz. Measurement of current-voltage relations in the membrane of the giant axon of loligo. *The Journal of Physiology*, 116(4):424–448, April 1952. PMID: 14946712 PMCID: PMC1392219.

[HMDH08] Steven Hughes, Stuart McBain, Jon Dobson, and Alicia J. El Haj. Selective activation of mechanosensitive ion channels using magnetic particles. *Journal of The Royal Society Interface*, 5(25):855–863, August 2008.

[HT08] Mark Howarth and Alice Y Ting. Imaging proteins in live mammalian cells with biotin ligase and monovalent streptavidin. *Nature protocols*, 3(3):534–545, 2008. PMID: 18323822 PMCID: 2671200.

[LFP+08] Sophie Laurent, Delphine Forge, Marc Port, Alain Roch, Caroline Robic, Luce Vander Elst, and Robert N. Muller. Magnetic iron oxide nanoparticles: Synthesis, stabilization, vectorization, physicochemical characterizations, and biological applications. *Chem. Rev.*, 108(6):2064–2110, 2008.

[LHJ+07] Jae-Hyun Lee, Yong-Min Huh, Young-wook Jun, Jung-wook Seo, Jung-tak Jang, Ho-Taek Song, Sungjun Kim, Eun-Jin Cho, Ho-Geun Yoon, Jin-Suck Suh, and Jinwoo Cheon. Artificially engineered magnetic nanoparticles for ultra-sensitive molecular imaging. *Nat Med*, 13(1):95–99, January 2007.

[LJC+11] Jae-Hyun Lee, Jung-tak Jang, Jin-sil Choi, Seung Ho Moon, Seung-hyun Noh, Ji-wook Kim, Jin-Gyu Kim, Il-Sun Kim, Kook In Park, and Jinwoo Cheon. Exchange-coupled magnetic nanoparticles for efficient heat induction. *Nat Nano*, 6(7):418–422, July 2011.

[Mas81] R. Massart. Preparation of aqueous magnetic liquids in alkaline and acidic media. *IEEE Transactions on Magnetics*, 17(2):1247– 1248, March 1981.

[Mat38] Carlo Matteucci. Sur le courant lectrique o propre de la grenouille. second memoire sur l'lectricit animale, faisant suite celui sur la torpille. *Ann. Chim Phys*, 67:93–106, 1838.

[MPGP07] Sasmita Mohapatra, Dibyarupa Pal, Sudip K. Ghosh, and Panchanan Pramanik. Design of superparamagnetic iron oxide nanoparticle for purification of recombinant proteins. *Journal of Nanoscience and Nanotechnology*, 7(9):3193–3199, 2007.

[MTC+00] va Mezey, Zsuzsanna E. Tth, Daniel N. Cortright, Michelle K. Arzubi, James E. Krause, Robert Elde, Athena Guo, Peter M. Blumberg, and Arpad Szallasi. Distribution of mRNA for vanilloid receptor subtype 1 (VR1), and VR1-like immunoreactivity, in the central nervous system of the rat and human. *Proceedings of the National Academy of Sciences of the United States of America*, 97(7):3655–3660, March 2000. PMID: 10725386 PMCID: PMC16295.

[MXC04] Magdalene M Moran, Haoxing Xu, and David E Clapham. TRP ion channels in the nervous system. *Current Opinion in Neurobiology*, 14(3):362–369, June 2004.

[NS76] Erwin Neher and Bert Sakmann. Single-channel currents recorded from membrane of denervated frog muscle fibres. *, Published online: 29 April 1976; | doi:10.1038/260799a0*, 260(5554):799–802, April 1976.

[N49] L. Nel. Influence des fluctuations thermiques a l'aimantation des particules ferromagnetiques. *Comptes Rendus de l'Acadmie des Sciences*, 228:664–668, 1949.

[PJW+03] Costas M. Pitsillides, Edwin K. Joe, Xunbin Wei, R. Rox Anderson, and Charles P. Lin. Selective cell targeting with light-absorbing microparticles and nanoparticles. *Biophysical Journal*, 84(6):4023–4032, June 2003. PMID: 12770906 PMCID: PMC1302982.

[Ros87] P. Roschmann. Radiofrequency penetration and absorption in the human body: Limitations to high-field whole-body nuclear magnetic resonance imaging. *Medical Physics*, 14(6):922–931, 1987.

[Ros02] R.E. Rosensweig. Heating magnetic fluid with alternating magnetic field. *Journal of Magnetism and Magnetic Materials*, 252(0):370–374, November 2002.

[SB83] Toshihide Sato and Lloyd M Beidler. Dependence of gustatory neural response on depolarizing and hyperpolarizing receptor potentials of taste cells in the rat. *Comparative Biochemistry and Physiology Part A: Physiology*, 75(2):131–137, 1983.

[SCDM08] Katarzyna Starowicz, Luigia Cristino, and Vincenzo Di Marzo. TRPV1 receptors in the central nervous system: potential for previously unforeseen therapeutic applications. *Current pharmaceutical design*, 14(1):42–54, 2008. PMID: 18220817.

[SENJ$^+$08] Amanda K. A. Silva, E. Scrates T. Egito, Toshiyuki Nagashima-Jnior, Ivonete B. Arajo, rica L. Silva, Luiz A. L. Soares, and Artur S. Carrio. Development of superparamagnetic microparticles for biotechnological purposes. *Drug Development & Industrial Pharmacy*, 34(10):1111–1116, October 2008.

[Shl74] M I Shliomis. Magnetic fluids. *Soviet Physics Uspekhi*, 17(2):153–169, February 1974.

[SISI87] Toshihiko Sato, Tetsuo Iijima, Masahiro Seki, and Nobuo Inagaki. Magnetic properties of ultrafine ferrite particles. *Journal of Magnetism and Magnetic Materials*, 65(23):252–256, March 1987.

[SLM09] Alexey Shavel and Luis M. Liz-Marzn. Shape control of iron oxide nanoparticles. *Physical Chemistry Chemical Physics*, 11(19):3762, 2009.

[SZR+03] Shouheng Sun, Hao Zeng, David B. Robinson, Simone Raoux, Philip M. Rice, Shan X. Wang, and Guanxiong Li. Monodisperse MFe2O4 (M = fe, co, mn) nanoparticles. *J. Am. Chem. Soc.*, 126(1):273–279, 2003.

[TMVV+06] Pedro Tartaj, Maria P. Morales, Sabino Veintemillas-Verdaguer, Teresita Gonzalez-Carreo, Carlos J. Serna, and K.H.J. Buschow. chapter 5 synthesis, properties and biomedical applications of magnetic nanoparticles. In *Handbook of Magnetic Materials*, volume Volume 16, pages 403–482. Elsevier, 2006.

[TT05] Makoto Tominaga and Tomoko Tominaga. Structure and function of TRPV1. *Pflgers Archiv European Journal of Physiology*, 451(1):143–150, 2005.

[VDW+04] Thomas Voets, Guy Droogmans, Ulrich Wissenbach, Annelies Janssens, Veit Flockerzi, and Bernd Nilius. The principle of temperature-dependent gating in cold- and heat-sensitive TRP channels. *Nature*, 430(7001):748–754, August 2004.

[Wei96] Thomas Fischer Weiss. *Cellular Biophysics, Vol. 2: Electrical Properties.* A Bradford Book, March 1996.

[YLQ10] Jing Yao, Beiying Liu, and Feng Qin. Kinetic and energetic analysis of thermally activated TRPV1 channels. *Biophysical Journal*, 99(6):1743–1753, September 2010. PMID: 20858418 PMCID: PMC2941006.

[You38] J. Z. Young. The functioning of the giant nerve fibres of the squid. *Journal of Experimental Biology*, 15(2):170–185, April 1938.

[ZLNM02] Boris V Zemelman, Georgia A Lee, Minna Ng, and Gero Miesenbck. Selective photostimulation of genetically chARGed neurons. *Neuron*, 33(1):15–22, January 2002. PMID: 11779476.

[ZM01] Boris V Zemelman and Gero Miesenbck. Genetic schemes and schemata in neurophysiology. *Current Opinion in Neurobiology*, 11(4):409–414, August 2001.